UV INSIGHTS INTO THE COMPLEX POPULATIONS OF M 87 GLOBULAR CLUSTERS[*]

A. BELLINI[1], A. RENZINI[2], J. ANDERSON[1], L. R. BEDIN[2], G. PIOTTO[2,3], M. SOTO[1], T. M. BROWN[1], A. P. MILONE[4], S. T. SOHN[5], A. V. SWEIGART[6]

Draft version April 30, 2015

Abstract

We have imaged with *HST*'s WFC3/UVIS the central $2.'7 \times 2.'7$ region of the giant elliptical galaxy M 87, using the ultraviolet filter F275W. In combination with archival ACS/WFC data taken through the F606W and F814W filters, covering the same field, we have constructed integrated-light UV−optical colors and magnitudes for 1460 objects, most of which are believed to be globular clusters belonging to M 87. The purpose was to ascertain whether the multiple-populations syndrome, ubiquitous among Galactic globular clusters (GCs), exists also among the M 87 family of clusters. To achieve this goal, we sought those GCs with exceptionally blue UV-to-optical colors, because helium-enriched sub-populations produce a horizontal-branch morphology that is well populated at high effective temperature. For comparison, integrated, synthetic UV−optical and purely optical colors and magnitudes have been constructed for 45 Galactic GCs, starting from individual-star photometry obtained with the same instruments and the same filters. We identify a small group of M 87 clusters exhibiting a radial UV−optical color gradient, representing our best candidate GCs hosting multiple populations with extreme helium content. We also find that the central spatial distribution of the bluer GCs is flattened in a direction parallel to the jet, while the distribution of redder GCs is more spherical. We release to the astronomical community our photometric catalog in F275W, F606W and F814W bands and the high-quality image stacks in the same bands.

Subject headings: galaxies: individual (M 87) — galaxies: star clusters: general — Galaxy: globular clusters: general — Hertzsprung-Russell and C-M diagrams — techniques: photometric

1. INTRODUCTION

In recent years the discovery and characterization of multiple stellar populations in globular clusters (GCs) has given a new impetus to GC studies, opening entirely new scenarios for their formation. First came the discovery that the main sequence (MS) of ω Cen splits into two, distinct parallel sequences (Bedin et al. 2004). Subsequent spectroscopic analysis showed that, instead of a lower metal abundance, the blue sequence has a *higher* metallicity compared to the red sequence, inescapably demanding that blue MS stars must be greatly enriched in helium (Piotto et al. 2005: see also Norris 2004). This is now quantified in $Y = 0.39$ (King et al. 2012), compared to the metal-poor population that is presumed to have near-primordial helium abundance ($Y \sim 0.24$).

Since then, evidence for multiple populations in GCs has rapidly accumulated, mainly thanks to the exquisite photometric accuracy of the Wide-Field Channel of the Advanced Camera for Surveys (ACS/WFC). NGC 2808 was found to

have three main sequences (Piotto et al. 2007), in spite of showing no dispersion in the abundance of iron-peak elements, again demanding that each MS have a different helium content, up to $Y \sim 0.40$. In addition, multiple sub-giant branches were found in several clusters (Milone et al. 2008; Piotto 2009; Piotto et al. 2012; Bellini et al. 2013), as well as a multiple main sequences (Milone et al. 2010, 2012ab, 2015; Bellini et al. 2013: Piotto et al. 2015).

Besides shaking the old paradigm of GCs as simple stellar populations, these findings raise three fundamental questions: 1) Is the multiple-population phenomenon a general property of GCs, no matter in which galaxy they are hosted today? 2) How were such multiple populations generated? 3) What is the origin of the helium enrichment? The answers to these questions have deep implications for our understanding of the formation of GCs, i.e., of objects that are still playing a pivotal role in so many astrophysical areas and especially for the early star formation in the Universe. Indeed, GC ages place their formation tantalizingly close to the epoch of re-ionization, to speculate they (or their precursors) may have had a part in it. Meanwhile, the discovery of multiple populations with large helium differences has shed new light on one long-standing mystery: the puzzling morphology of the horizontal branch (HB) and its poor correlation with cluster metallicity, an issue that, after van den Bergh (1967), is traditionally referred to as the *Second Parameter* problem. Indeed, the helium abundance has strong control over the range of effective temperatures covered by stars during their HB phase, with higher helium leading to higher effective temperatures for HB stars, hence brighter cluster UV luminosities. Thus, high-helium multiple main sequences are associated with multimodal distributions of stars on the HB, with prototypical examples being offered by ω Cen and NGC 2808. Multimodal HB distributions offered in fact the first hint for high-helium sub-

bellini@stsci.edu

[*] Based on proprietary and archival observations with the NASA/ESA Hubble Space Telescope, obtained at the Space Telescope Science Institute, which is operated by AURA, Inc., under NASA contract NAS 5-26555.

[1] Space Telescope Science Institute, 3700 San Martin Drive, Baltimore, 21218, MD, USA

[2] INAF – Osservatorio Astronomico di Padova, vicolo dell'Osservatorio 5, 35122 Padova, Italy

[3] Dipartimento di Fisica e Astronomia 'Galileo Galilei', Università di Padova, Vicolo dell'Osservatorio 3, 35122 Padova, Italy

[4] Research School of Astronomy & Astrophysics, Australian National University, Mt Stromlo Observatory, via Cotter Rd, Weston, ACT 2611, Australia

[5] Department of Physics and Astronomy, The Johns Hopkins University, 3400 North Charles Street, Baltimore, 21218, MD, USA

[6] NASA Goddard Space Flight Center, Exploration of the Universe Division, Code 667, Greenbelt MD 20771, USA

populations in NGC 2808 (D'Antona & Caloi 2004), which was then confirmed by the *HST* discovery of multiple main sequences in the same cluster (Piotto et al. 2007).

Most clusters with multiple populations are chemically homogeneous in iron and other heavy elements, which implies that helium enrichment and CNO processing have proceeded without being contaminated by supernova products. This excludes in most cases massive stars ($M \gtrsim 10\ M_\odot$) from having been involved in the chemical enrichment of secondary populations, in either their fast rotating (e.g., Krause et al. 2013) or binary (de Mink et al. 2009) versions (e.g., Renzini 2008, 2013, for critical reviews). This leaves intermediate-mass AGB stars as possible sources of the helium-enriched and p-capture processed material out of which second generations would have been formed. However, the AGB scenario is also far from providing a detailed description of the sequence of events leading to GCs and their multiple populations as we see them today. Particularly intriguing is the mass budget requirement in this scenario, as the first generation delivers only $\sim 5\%$ of its mass as AGB ejecta, whereas secondary populations in GCs tend to be nearly as massive as –or even more massive than– the first generation. Thus, for the first generation to produce enough AGB ejecta (to account for the mass of secondary generations) it should have been at least ~ 20 times more massive than its fraction still bound to the cluster. This is indeed a lower limit, as it assumes 100% efficiency in converting AGB ejecta into second-generation stars. Thus, in this scenario precursors to present-day GCs should have been much more conspicuous objects than their surviving remnants.

A mechanism that in principle could alleviate this mass-budget problem is accretion of AGB ejecta on stars belonging to the same (first) generation, a process first proposed to account for the composition anomalies known at that time (D'Antona et al. 1983; Renzini 1983), and now still entertained in the modern context (Bastian et al. 2013). However, accretion will inevitably differ from star to star, hence may produce some spread in chemical composition, but cannot generate discrete, *quantized* sub-populations (Renzini 2013), such as e.g., the seven or so seen in ω Cen (Bellini et al. 2010) or the three seen in NGC 2808 (Piotto et al. 2007). Actually, recent WFC3/UVIS data reveal the presence of at least five distinct populations in NGC 2808, while M 2 exhibits at least seven of them (Milone et al. 2015). This discreteness of multiple populations is an extremely powerful discriminant for the various scenarios proposed for the origin of multiple populations, excluding those which for their very nature are incapable of producing discrete, distinct populations. For example, in the fast-rotating-massive-star option (e.g. Krause et al. 2013 and references therein) stars of secondary populations would form in the extruding disk of massive stars, with each massive star delivering secondary stars with a range of abundances. Globally, just a spread of compositions would result. Moreover, membership into GCs of fast rotating massive stars would be irrelevant for the production of secondary stars, which then should be equally abundant in GCs as in the Galactic halo field, contrary to observations (Renzini 2013). Discreteness of secondary populations therefore demands discrete star formation events, such as a series of star-formation bursts out of an interstellar medium (ISM) whose composition is slowly changing, interleaved by phases during which the mass of the ISM grows thanks to the ejecta from the first generation.

In any event, the requirement of a 20–100 times more massive precursor to present day GCs remains valid in the AGB scenario, thus making GC formation a major event in the early stages of galaxy evolution. Such precursors may have been dwarf nucleated galaxies, 10^7–$10^8\ M_\odot$ by mass in which, past the supernova era, the AGB ejecta stream to the bottom of the potential well in a sort of *cooling flow* to form the secondary populations, such as e.g. in the models of D'Ercole et al. (2010, 2011). In these models most of the stars of the parent dwarf are later stripped by tidal interactions, thus leaving the bare nucleus with its multiple populations. One pressing question is whether this process of GC formation requires special environmental circumstances, which may be present in one (proto)galaxy but not in others. In our own Milky Way (MW), the multiple-population syndrome is virtually ubiquitous among GCs (Piotto et al. 2015), but what about other galaxies? And especially, what about very massive elliptical galaxies with their thousands of GCs? It is indeed quite important for our understanding of GC formation to establish whether the presence of multiple populations is a generic property of GCs, irrespective of the type and mass of the parent galaxy, or whether a special environment (parent galaxy) is required. To answer this question one will have to rely on integrated light observations, as resolving stars in GCs is not currently feasible for distances beyond the Local Group.

The existence of helium-enriched sub-populations can be inferred from the presence of extremely hot HB stars (EHB), which dominate the UV luminosity of clusters containing them in sufficient numbers. Typical in this respect are the metal-rich clusters NGC 6388 and NGC 6441 that belong to the Galactic bulge, where the existence of EHB stars was first inferred from their blue UV−optical colors and then confirmed by *HST* photometry (Rich et al. 1997; Busso et al. 2007). In this way, the integrated UV−optical colors of GCs were thought to offer a unique opportunity to infer the existence of helium-rich sub-populations in distant, unresolved GCs belonging to galaxies of various morphological types, which cannot be resolved into individual stars. In this mood, the bluer the UV−optical color at a given $V - I$ color, the stronger the EHB component, and especially so for the reddest $V - I$ clusters. A first such experiment was attempted by Sohn et al. (2006, hereafter S06) and Kaviraj et al. (2007, hereafter K07) for the giant elliptical M 87, the cD galaxy of the Virgo cluster. These authors used STIS FUV (covering the 1150–1700 Å range) and NUV (1600–3100 Å range) data in combination with optical photometry to infer the likely existence of helium-rich sub-populations in a small group of GCs in M 87. The presence of a very strong EHB component in these clusters was inferred from their extremely blue UV−optical colors FUV − V and NUV − V for a given $V - I$. In these studies M 87 GCs appear to be even more UV-strong than the bluest Galactic GCs with helium-rich populations, thus suggesting that the multiple-population syndrome is spread also among GCs in this giant elliptical.

The S06 and K07 studies have opened the tantalizing opportunity to diagnose the presence of (likely) helium-enriched extreme EHB stars in very distant globular clusters, and in particular in a giant elliptical galaxy. Yet, their sample includes only 66 M 87 clusters, due to the very small area covered by the STIS observations (just ~ 2540 arcsec^2). Moreover, for the reference population, they had to rely on early integrated-light UV observations of Galactic GCs, namely with the *Astronomical Netherlands Satellite* (van Albada et al. 1981), with different UV passbands and calibrations compared to the

STIS data used for the M 87 GCs.

For these reasons, we submitted a *HST* proposal (GO-12989, PI: A. Renzini) to observe the central part of M 87 with the Ultraviolet-VISible channel of the Wide-Field Camera 3 (WFC3/UVIS) in the F275W band, exploring in a single shot an area over 10 times larger than that covered by the STIS observations and reaching substantially fainter objects. Moreover, for our reference population, we can also use WFC3/UVIS ultraviolet data for both M 87 and the MW GC systems, thus avoiding passband differences and calibration issues when comparing M 87 and MW clusters. The complementary archival optical data consists of very deep (50 orbits) archival F606W and F814W ACS/WFC imaging of the central region of M 87 (GO-10543, PI: E. A. Baltz).

Thus, the plan of the project was to construct UV−optical color-magnitude diagrams and a $m_{F275W} - m_{F606W}$ and $m_{F275W} - m_{F814W}$ vs. $m_{F606W} - m_{F814W}$ two-color diagrams to characterize the UV properties of a large, representative sample of GCs in M 87. Our aim was then to address the following questions:

- Is the presence of helium-enriched GC sub-populations as widespread (or more so) in a giant elliptical compared to the Milky Way?

- Has environment (present parent galaxy type) affected the GC formation process by favoring/disfavoring the formation of multiple stellar generations?

- Is the frequency of UV-bright GCs different among the blue/red component of the bimodal color (metallicity) distribution of GCs in a giant elliptical such as M 87?

- Is there a connection between the UV-bright populations in GCs and the UV-upturn in elliptical galaxies?

However, answering these questions proved to be more difficult than we expected. Indeed, the *HST* F275W data acquired in the meantime for a large sample of MW GCs (Piotto et al. 2015) show that the above UV−optical two-color plots are not able to provide unambiguous evidence for the presence of an EHB component. Still, the UV data on the M87 and MW GCs are used to highlight possible systematic differences between the two cluster families. UV−optical color gradients within the brightest M 87 clusters are also used to tentatively find evidence for the presence in them of helium-enriched EHB stars.

The paper is organized as follows. Sections 2 and 3 describe the *HST* data reduction and processing. The photometric measurement of GCs in M 87 is presented in Section 4 while Section 5 deals with the completeness of the sample. Section 6 presents the color-magnitude and two-color plots for the M 87 globulars, whose spatial distribution is discussed in Section 7. Section 8 offers an extensive comparison with the Milky Way GCs and Section 9 investigates the possibilities of the detection of internal color gradients within individual GCs. Finally, in Section 10 we present and discuss our interpretation of the data and our conclusions.

2. DATA SETS AND PRELIMINARY REDUCTION

As mentioned earlier, this work is based on the WFC3/UVIS data from GO-12989 and on the ACS/WFC data from GO-10543 providing _flt-type images[1] of the core

of M 87. These data sets consist of $20 \times 1365\,s$ exposures taken through the WFC3/UVIS F275W filter and $58 \times 500\,s$ ACS/WFC F606W exposures plus $226 \times 360\,s$ ACS/WFC F814W exposures. All _flt images were corrected for charge-transfer efficiency defects (e.g., Anderson & Bedin 2010) using either the standard *HST* calibration pipeline (for ACS), of the official FORTRAN routine developed for the WFC3[2].

The initial catalog of sources in the ACS/WFC exposures was obtained using the publicly-available FORTRAN program img2xym_WFC.09x10, which is described in detail in Anderson & King (2006). The program employs empirical "library" effective point-spread functions (ePSFs) that vary spatially across the detector. Source positions and fluxes on WFC3/UVIS images were measured with the software program img2xym_wfc3uv, derived from img2xym_WFC.09x10, which also employs library, spatially-varying ePSFs. Both ACS and WFC3 software identify a source if its central pixel is brighter than the surrounding 8 pixel, regardless of the actual shape of the source (point-like, diffuse, etc.). Source positions in each single-exposure catalog were then corrected for geometric distortion using the state-of-the-art solutions provided by Anderson & King (2006) for ACS/WFC and by Bellini & Bedin (2009) and Bellini, Anderson & Bedin (2011) for WFC3/UVIS.

Even though M 87 GCs are slightly resolved by *HST* –and therefore a PSF is generally not an optimal representation of their light profiles– ePSF-derived positions for bright GCs are still found to be accurate to ~ 0.02 pixel.

3. IMAGE STACKS

Our final photometry was obtained from high-quality image stacks. Photometry on the stacks will allow us to obtain a more reliable measure for fainter sources, and to push down the detection limit by $\sim$1.6, 2.2 and 3 mag for F275W, F606W and F814W, respectively.

The preliminary single-exposure catalogs have been used only to setup a common distortion-free reference frame and to define the linear-transformation parameters that map each pixel of each exposure onto the image stacks. We based our reference frame on the F275W exposures, and we supersampled its pixel size by a factor of 2. This means that each pixel on the stacks corresponds to 20 mas. In order to accommodate all meaningful pixels on the stacks, we shifted the rough center of M 87 (as defined by the telescope pointing) to location (5000, 5000) on the master frame. We identified common sources in each single exposure and used their distortion-corrected positions to compute general 6-parameter linear transformations to map each pixel of each exposure on to the master frame.

Although the F275W exposures are each over 22 minutes long, only a few dozen sources are clearly detected in each of them. Moreover, due to the length of these exposures, each F275W image is deeply contaminated by thousands of cosmic-rays, many of which got included in the single-exposure catalogs as real objects. (Cosmic-ray events are far less abundant in F606W or F814W images, given their shorter exposure times.) Special care was dedicated to identifying common sources between the catalogs to obtain the best linear-transformation coefficients using only real sources. To

---

[1] _flt images are produced by the standard *HST* calibration pipeline *CALWF3* (for WFC) or *CALACS* (for ACS). Images of type _flt are dark-

and bias-subtracted and flat-fielded, but not resampled (like the _drz-type images).

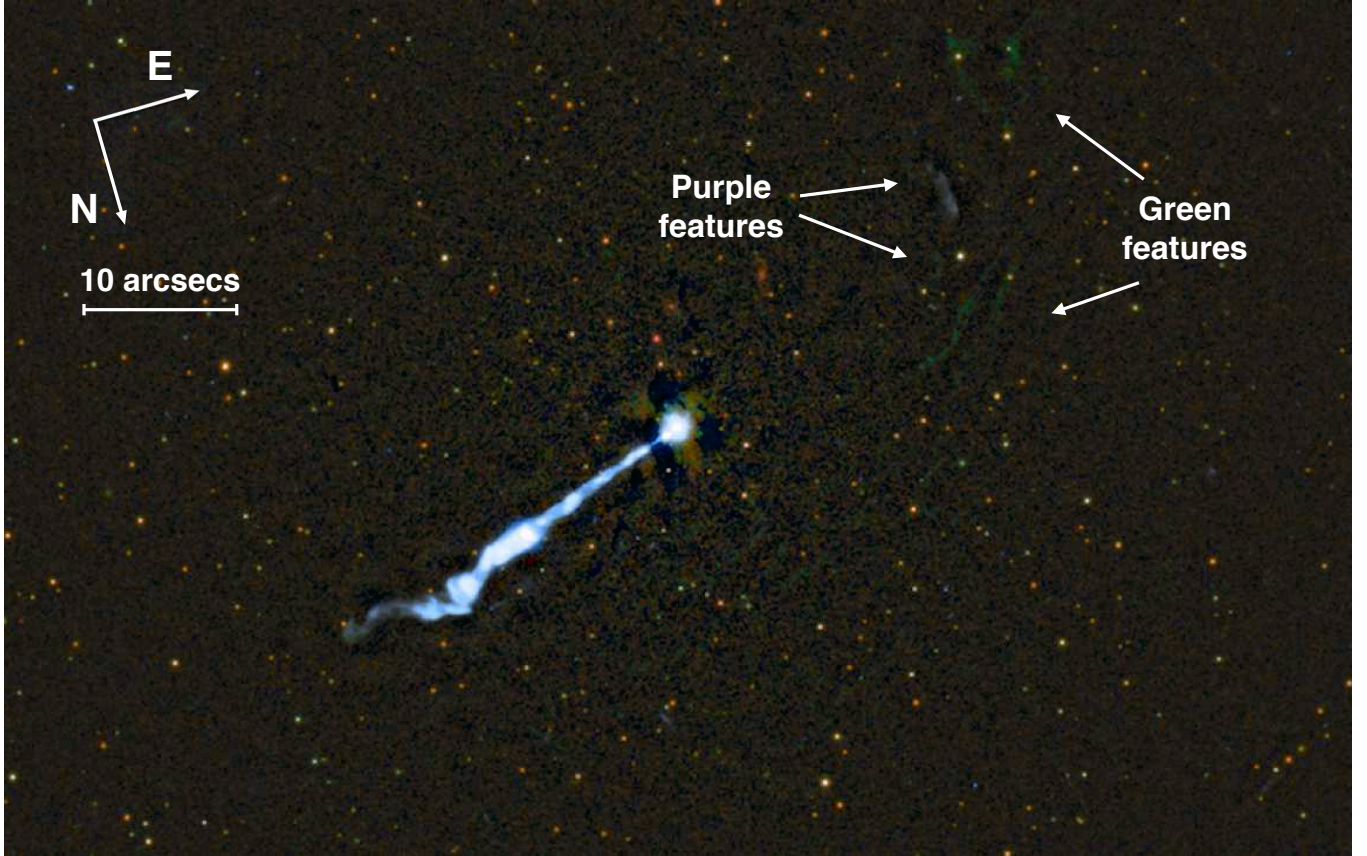[2] http://www.stsci.edu/hst/wfc3/ins_performance/CTE/.

Figure 1. The galaxy-subtracted, trichromatic image obtained by combining F275W, F606W and F814W stacks. The color scale has been stretched to enhance faint sources and maximize the color difference between blue and red globular-cluster candidates. The vast majority of the individual sources are indeed globular clusters in M 87. Some counterjet features are also highlighted. These and other features are briefly discussed in the dedicated Appendix. Note that this is a high resolution image and some of these faint features are better seen by enlarging the image on the screen.

this aim, we made use of the quality-of-fit parameter (Anderson et al. 2008) in order properly select the best-measured objects for the linear transformations. At this point, all the necessary pieces of information required by the stacking algorithms were collected, and we proceeded with the construction of the image stacks themselves.

Our WFC3/UVIS exposures in F275W were properly dithered with an image-stacking strategy in mind. Unfortunately, dithering in the archival data was minimal. This means that bad columns, hot/cold pixels, and other detector defects are often present at the same place in the field in multiple exposures and cannot simply be "sigma-clipped" away. Therefore, before we could create a stack that was representative of the astronomical scene, we had to first identify the warm/hot pixels. Unfortunately, the DQ flags[3] did not identify all the warm pixels, so we had to first stack the dithers independently, then compared each exposure against the stacks made from the other dithers in order to identify the inconsistent pixels. We compared each exposure against the stack made from other dithers and flagged each time a particular pixel was inconsistent at the 5σ level with the prediction from the comparison stack. We then flagged as bad any pixel that was flagged in more than half of the exposures. This allowed us to identify the bad pixels and construct stacks in F606W and F814W that were free of artifacts.

Since the goal of this program was to perform aperture pho-

tometry on M 87's globular clusters, we constructed the stacks in such a way as to carefully preserve flux. We mapped the four corners of each pixel in each exposure into the reference frame and determined the geometric overlap between each input pixel and each output pixel (in the stacked frame). These weights were used to construct the output image. Bad pixels were naturally given zero weight. This procedure results in a small amount of blurring, but this should have a negligible effect on our photometry given the $\times 2$ oversampling used and the relatively large apertures we used.

Since each exposure can have a slightly different sky level, on account of variations in scattered light, we iterated the stacking procedure. After each iteration, we resampled the stacked image into the frame of each individual exposure. This allowed us to determine an average sky offset between each exposure and the average of all of them. We then adjusted the background level of each exposure by this difference. This converged after two iterations and the procedure was used to generate a stack for the F275W, F606W and F814W exposures.

The cD galaxy in our field introduces a considerable gradient in our stacks. Since our focus is on the clusters, we decided to iteratively remove this gradient to make background subtraction trivial. We parametrized the background by its value at an array of 106×106 elements across the $10\,500 \times 10\,500$-pixel frame. In other words, we had one array value every 100×100 pixels. We iteratively solved for the array that reduced the background to zero everywhere, using a Zeno factor of 0.5 and 16 iterations. The background was

---

[3] Each pixel of the _flt exposures has an associated data-quality (DQ) flag that allows the user to discriminate between good and bad pixels.

smooth enough to use linear interpolation everywhere.

Figure 1 shows the central region of M 87 on our galaxy-light-subtracted trichromatic stack. The vast majority of near point-like sources in the figure are M 87 GCs and the color scale has been stretched to emphasize the color difference between blue and red GC candidates. The granularity of the background in close proximity of the galactic center is mostly caused by background noise, but far from the center the noise is low enough to clearly reveal surface-brightness variations in the light profile of M 87. The famous jet is prominent in this figure and various counterjet features are also apparent. The study of the jet and related features goes beyond the scope of the present paper, but we briefly discuss them in the Appendix.

4. PHOTOMETRY OF INDIVIDUAL SOURCES

As already mentioned in Section 2, M 87 GCs are partially resolved, making PSF-fitting techniques not appropriate for high-precision photometry. Therefore, we applied standard aperture photometry to measure the flux of the M 87 GCs.

The finding process was performed on the F814W stack only: this stack is made by the largest number of single exposures, and it should therefore be the one with the highest signal-to-noise ratio. We identified all pixels in each exposure that were local maxima (larger than their 8 surrounding neighbors) and were more than 2.5 times the rms of the background noise. We ignored areas of the field where there was fewer than 3 exposures' depth.

A total of 2155 qualifying peaks were found this way. A visual inspection of their locations on the F814W stack allowed us to remove spurious objects (mostly obvious galaxies and stars) from the list, leaving 1913 GC candidates. Aperture photometry was then performed at these locations on the three image stacks, using a circular aperture with a 7-pixel radius ($0.\!''14$). The local sky was estimated between 15 and 20 pixels. The choice of using a 7-pixel aperture is motivated by the fact that it encircles the most-significant pixels of typical M 87 GCs (being slightly-resolved sources which typical FWHM of $\lesssim 5$ pixels). A larger aperture would have made our photometry too sensitive to random background fluctuations, especially for the faint sources in F275W. For the brightest GCs in M 87, a larger aperture is more appropriate. A 15-pixel aperture for these objects is applied and discussed in Section 8.1.

All of the 1913 objects have positive measured fluxes in F814W and F606W, and 1460 of them also had positive fluxes in the F275W stack, making our UV photometry by far the largest available in the literature for extra-galactic GCs. Finally, the photometry in the three bands was calibrated into the Vega-mag flight system following Sirianni et al. (2005), and using the F275W zero point and aperture correction provided by the STScI webpage[4].

A visual inspection of the F275W image stack revealed the presence of a handful of relatively bright UV objects that were not identified in the F814W stack. These objects are likely transient sources in M 87, such as novae, or UV-bright background galaxies. Since our aim is to study M 87 GCs, we will not consider them further in this paper.

5. COMPLETENESS

In order to infer the completeness level of our source list, as well as to estimate photometric errors, we ran extensive arti-

---

[4] http://www.stsci.edu/hst/wfc3/phot_zp_lbn.

ficial GC tests. For the simulated GCs we used 2D Gaussians with a full width at half maximum of 4.5 pixels, which is the average value found for M 87 GCs.

While it is true that our stacks are made in such a way to preserve both source positions and fluxes, the actual shape of the GCs in the stacks is the average of several, uncorrelated PSFs (due to different telescope-breathing conditions for each exposure). Thus, a 2D Gaussian turned out to be a fair representation of these average PSFs while accounting also for GCs of M 87 not being point-like sources.

Instead of the usual practice of simulating GCs with magnitudes and colors following the cluster fiducial sequences on the CMDs, we populated the full color-magnitude diagram (CMD) space occupied by the real GCs with nearly 17 million sources, and assigned to them a random position on our stacks. Note that M 87 GCs span over 6 magnitudes in the $m_{\mathrm{F275W}} - m_{\mathrm{F814W}}$ color, hence this approach allows us to better estimate incompleteness and photometric errors across such a wide color range. As for the real GCs, the finding process was performed only on the F814W stack. We added one simulated GC at a time, and determined whether its central pixel qualifies as a peak. If so, we measured its flux using a 7-pixel-radius aperture photometry in all three stacks. Before moving to the measurement of the next artificial object, we removed the current simulated GC from the stacks. This way, simulated GCs never interfere with each other, but only with the real sources of the stacks, as it should be.

We consider a simulated GC to be recovered if its measured position in the F814W stack was within 0.75 pixel of the input position, and if its measured photometry was within 0.75 mag of its input photometry in each of the three bands. There was no need to impose a position constraint on the F275W and the F606W recovered magnitudes since, exactly as we have done for the real GCs, their positions are defined by the measured centroids on the F814W stack. Finally, the completeness level was simply obtained as the ratio between the number of recovered GCs and the number of input GCs.

To estimate the photometric errors, we computed the 68.27^{th} percentile (rms) of the absolute values of the difference between input and output magnitudes. These rms values represent our estimate of the photometric uncertainties. The results of the artificial GC tests are summarized in Figures 2 and 3. The CMDs of real sources (black squares) are shown Figure 2, one for each color-filter combination at our disposal. In each CMD we divided the simulated GCs in thousands of small regions (each containing hundreds of input sources), and we determined the completeness level for each of them. Each region is then color-coded according to its measured completeness. The color ranges from red (0%) to yellow (100%). A color bar on top of the first panel illustrates the adopted color-coding, which is kept the same in all panels. Nine contour lines indicate the loci of average 10% to 90% completeness level, with the 50% contour line being heavier than the others, for clarity. The contour lines in the optical CMD are almost horizontal, meaning that, within the investigated color range, the completeness level of sources measured in the F814W and F606W stacks is similar, with the F606W stack actually going a little deeper than that of F814W one. This is not the case for the UV CMDs, where the completeness level of the sources measured in F275W drops appreciably towards the red part of the CMDs.

The CMD in which the incompleteness effects are most evident is the $m_{\mathrm{F275W}} - m_{\mathrm{F606W}}$ one, where sources have to be
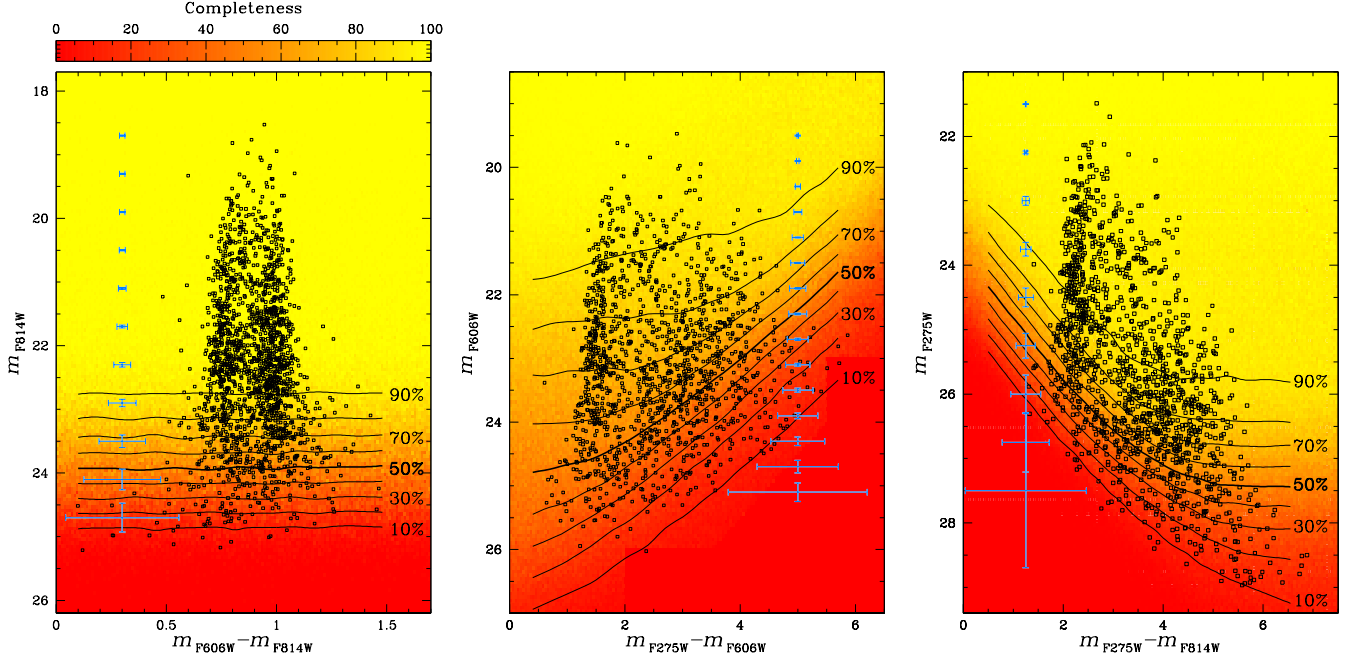
Figure 2. The three color-magnitude diagrams for the individual sources in the M 87 field. The background is color-coded from red (0%) to yellow (100%) according to the measured completeness level. Photometric error bars, also inferred from the completeness analysis, are shown in light blue. Completeness percentiles are in black.

found in all the three bands. The typical size of the photometric errors are also shown, in light blue and for sources of average color, in each CMD. Larger photometric errors are found, as expected, for F275W measurements. We will discuss these CMDs in detail in Section 6.

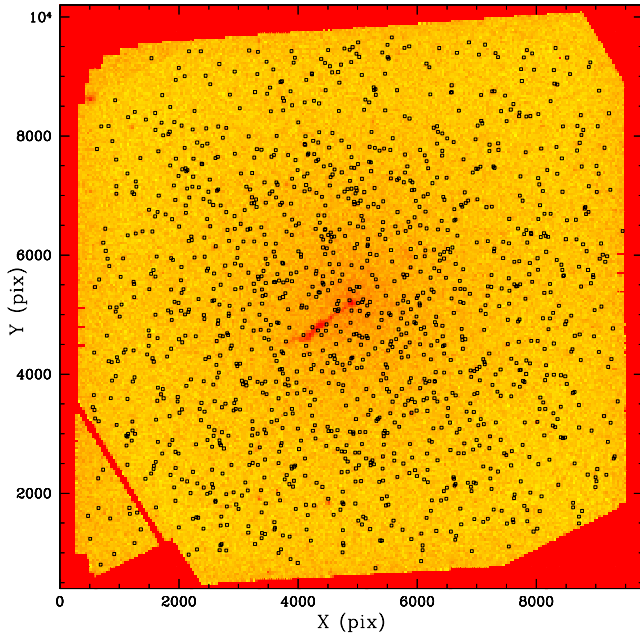Finally, Figure 3 shows the spatial F814W completeness

Figure 3. The spatial completeness map over the entire field of view, color coded as in the previous figure, for the F814W filter. GCs measured in all three bands are in black. The completeness level decreases toward the galaxy center, and in particular around the jet, where it averages 30% in its close proximity.

map indicating which parts of M 87 suffer from higher incompleteness levels regardless of the magnitude level. We adopted the same color-coding as in Figure 2. As expected, the completeness drops towards the center due to the higher background noise. The completeness level is also low around the jet, the location of which can be glimpsed even in this completeness map. The outer edges of this panel are not mapped by the minimum number of 3 exposures, and no artificial GCs were added there. A red color code (0% completeness) is applied to these marginal regions as well.

6. COLOR-MAGNITUDE AND TWO-COLOR DIAGRAMS

Figure 4 shows the CMDs of M 87's GCs using the three available color combinations (panels a, b and c), as well as the combined two-color diagram (panel d). The well-known color bimodality of M 87 GCs (e.g., Gebhardt & Kissler-Patig 1999) is clearly visible in all the CMDs. While the two GC sequences have a similar spread in $m_{F606W} - m_{F814W}$, the blue sequence is significantly narrower and more defined than the red one in $m_{F275W} - m_{F606W}$ and $m_{F275W} - m_{F814W}$. This effect is related to the increased photometric errors in F275W for the red GCs[5]: the color separation between the two GC sequences in the UV CMDs is ~ 2 magnitudes, meaning that, at a given m_{F606W} luminosity, red clusters are about 6 to 7 times fainter in F275W –on average– than their blue counterparts.

Six detected objects fall outside the red limit of panel (a), being redder than $m_{F606W} - m_{F814W} = 1.6$ (color-coded in red in the other panels of Figure 4). They also occupy a well-defined region in the two-color diagram of panel (d). A deeper inspection of their images on the stacks suggests they are compact passive galaxies at high redshifts and we will not consider them any further in this paper.

A quick look at panels (b) and (c) of Figure 4 also reveals the presence of a group of 25 extremely-blue objects, and we

[5] This effect is far better seen in Figure 5, rather than Figure 4, given the more favorable scale and aspect ratio.
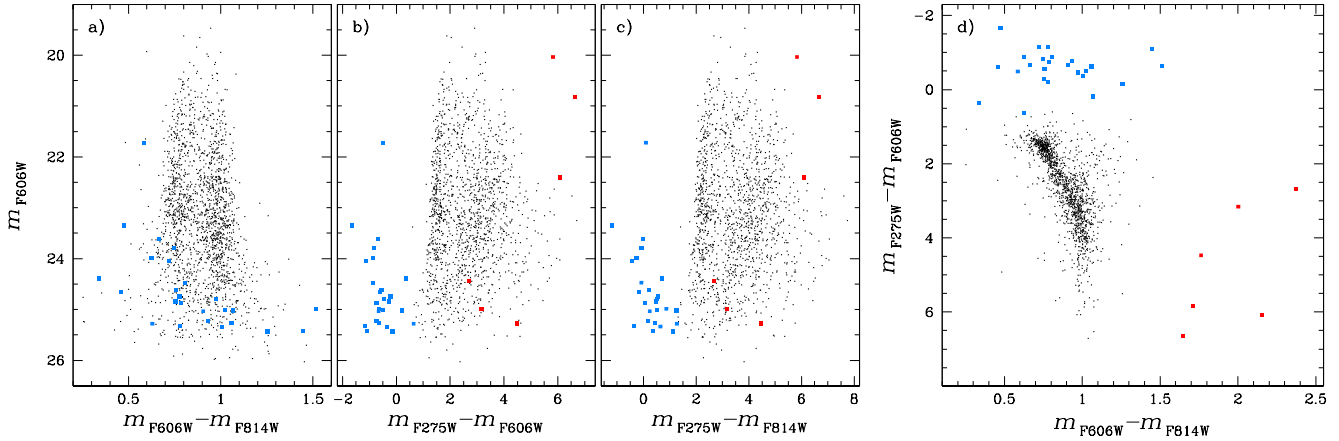
Figure 4. The optical and UV–optical color-magnitude diagrams of the sources in the M 87 field (panels a to c) with highlighted in blue and red the objects excluded from further discussion, being considered star-forming compact galaxies at moderate redshift the formers, and compact passive galaxies the latters. Panel (d) shows the two-color plot of the same sources.

color-coded them in blue in all the panels of the figure. It is worth noting that these very blue objects seem randomly placed in the optical CMD, and only the UV photometry allows us to single them out. These very blue objects occupy a well defined, isolated region in the two-color diagram shown in panel (d). Most of these blue objects are faint and appear quite compact in the trichromatic stack: we consider them to be small star-forming galaxies at moderately high redshift ($z \lesssim 2$), as they are not F275W *dropouts*. Hereafter, we will remove also these 25 objects from our analysis and therefore we are now left with 1882 likely M 87 GCs, with 1429 of them having also the F275W photometry.

Let us now turn our attention on the two-color diagram; a zoomed-in view of it can be seen in panel (a) of Figure 5. The inset shows a Hess diagram in which two main clumps are clearly visible. There is also a hint for a third, less prominent clump in between the main two ones, located approximately at (0.85, 2.5). The three clumps are marked with arrows. Panel (a) is replicated in panel (b) where we decided to arbitrarily split the sample into four groups according to their location in this plot. The *blue* GC component (508 objects, hereafter bGC) occupies a well-defined and compact region in the top-left corner of the panel, while the *red* component (731 objects, hereafter rGC) is more spread and stretches across increasing $m_{F275W} - m_{F606W}$ values while keeping a roughly constant optical color. The *intermediate* objects (117 by number, hereafter iGC) that seems to stand out in the Hess diagram are colored in yellow and appear to be offset in $m_{F606W} - m_{F814W}$ color with respect to the red component (indeed, they seem to follow the blue-component trend rather than the red-component trend), and are separated by a less-populated part of the Hess diagram at $(m_{F275W} - m_{F606W}) \simeq 2.2$ from the blue component itself. Finally, a small number of objects, colored in green, occupy the top-right region of the panel (73 objects, hereafter fGC). We stress that the definition of the intermediate GC component is arbitrary, and only marginally supported by the relative clump in the two-color diagram. Still, we will keep this four-group classification through the paper, and see whether the analyses presented in the next sections are able to support (or disprove) the presence of iGCs as a truly distinct group of clusters in M 87.

Turning now our attention to the lower three panels, we can notice that while bGCs, iGCs and rGCs are always to the left, middle and right side of these CMDs, respectively, fGCs are

redder –on average– than rGCs in the $m_{F606W} - m_{F814W}$ CMD, while they become as blue as the bGCs in $m_{F275W} - m_{F606W}$, and of somewhat intermediate color between bGCs and iGCs (but definitely bluer that rGCs) in $m_{F275W} - m_{F814W}$. Hence they *flip* in color. If the fGCs had been to be among the brightest GCs, we would have immediately found the best candidates for the helium-enhanced, multiple-population GCs, as the most prominent EHB extensions are found among the most massive GCs in the Milky Way. Alas, these fGCs are too faint to be the M 87 equivalent of, e.g., ω Cen or NGC 2808 (more in Section 8). We looked at each of them on the trichromatic stack, and their shapes appear to be essentially indistinguishable from those of the surrounding GCs of the same optical brightness level. Their average FWHM is also the same as that of the other clusters. Moreover, they are also rather isolated, so that light contamination from brighter neighbors is excluded.

Because fGCs are faint in all bands, the reader can argue that we are just trying to over-interpret what are just simply photometric-error effects. While it is true that the larger photometric error of fGCs can in principle explain their larger spread in the CMDs, they are never really randomly scattered among the other groups, but are always clumped in specific regions in each CMD. Nevertheless, most of these objects are so dim in m_{F275W} that, at the faint limit, their total flux amounts to only 10 electrons above the sky background in the F275W stack (sky noise of ~ 1.3 electrons). The fGCs could be just faint rGCs with large errors in the F275W flux. An intriguing possibility is that the fGCs are diffuse star clusters, such as those discovered by Larsen & Brodie (2000) around two lenticular galaxies, and already found in the Virgo cluster (Peng et al. 2006)[6]. However, having measured the size of all clusters with $23 < m_{F814W} < 24$ we found no difference between fGCs and the other clusters. Another, perhaps more likely possibility, is that they are not GCs at all, but compact emission-line galaxies at moderate redshifts. Nothing really conclusive can be said about fGCs until deeper F275W photometry becomes available.

The top panels of Figure 6 show the histograms of the color distribution for the three CMDs of Figure 5. We applied a smoothed naïve estimator (Silverman 1986) for the results

---

[6] Note that Peng et al. (2006) do not mention M 87 as harboring a significant number of diffuse star clusters, but their observations are much shallower than ours.
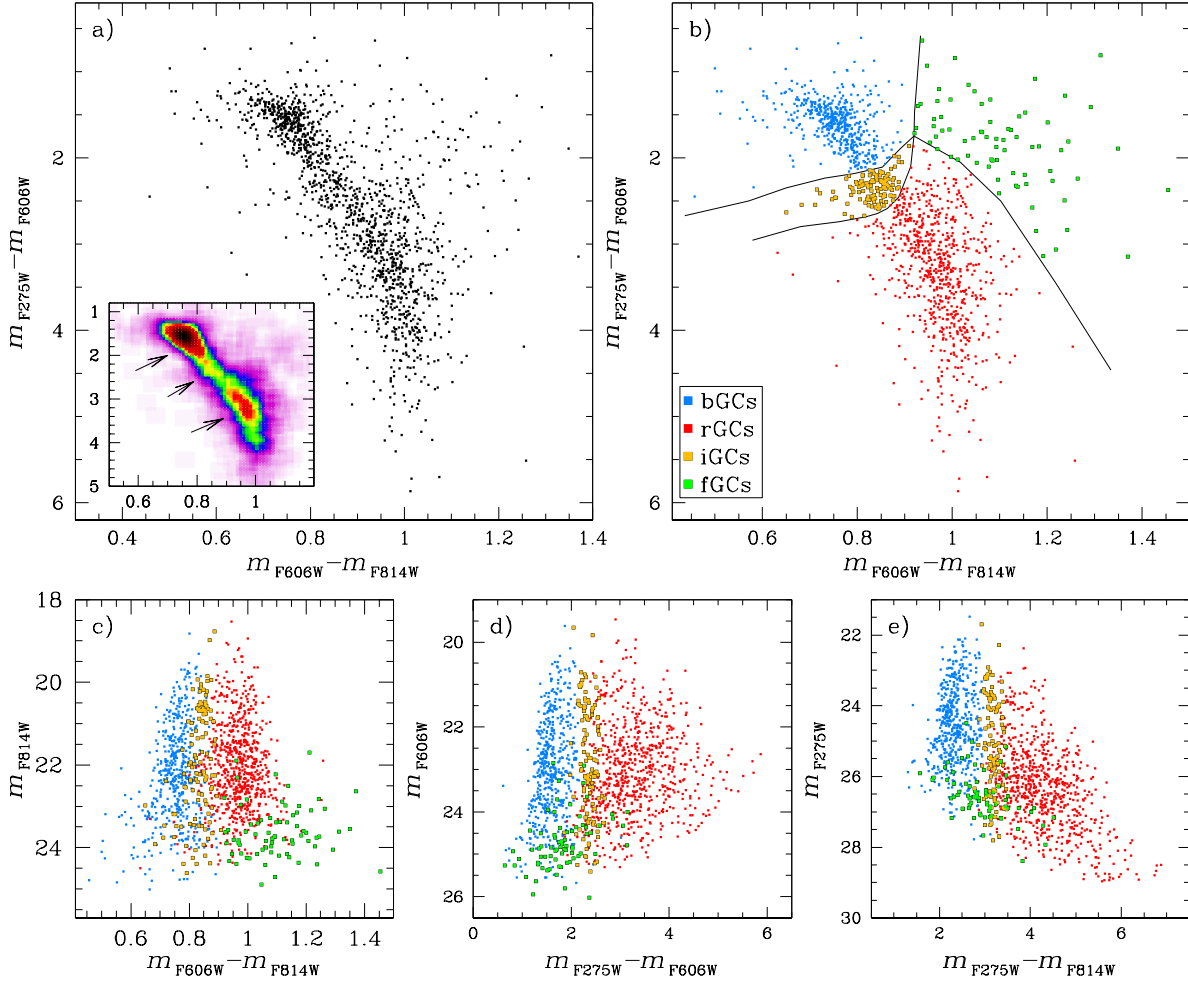
Figure 5. Panel (a) shows the two-color diagrams of M 87 GCs. Blue GCs clump at (0.75, 1.5) in this plane, while rGCs are more spread and stretch across increasing $m_{F275W} - m_{F606W}$ values while keeping a roughly constant optical color: an effect driven by the increasing F275W errors. An intermediate clump of GCs, at about (0.85, 2.5), seems to define an intermediate group of GCs (although their significance is statistically marginal). The inset shows a Hess diagram in which the three clumps are marked with arrows. An extended tail of GCs is present in the top-right quarter of the panel. Panel (b) is a replica of the previous panel, in which we show the regions used to arbitrarily divide M 87 GCs in 4 groups. The bottom panels (c), (d) and (e) show the CMDs of the four groups, color-coded as in panel (b).

to be insensitive to a particular binning starting point. Two peaks are clearly distinguishable in panel (a1) referring to the $m_{F606W} - m_{F814W}$ color distribution, with similar width. The Poisson errors are highlighted by shaded regions, and give an assessment of the quality of the peak detections. In panels (b1) and (c1) for the UV−optical colors the blue peak is very sharp, while red GCs are more spread in color and apparently show more than one peak. We divided the $m_{F606W} - m_{F814W}$ histogram in two halves as shown in panel (a2), color-coded in blue and red. This represents the classical bimodal subdivision. We identified the GCs belonging to each component and color-coded accordingly their histograms in panels (b2) and (c2). The blue histograms in the middle and right panels both show a secondary peak at redder colors. The significance of this second peak is marginal, yet it is present in both the $m_{F275W} - m_{F606W}$ and $m_{F275W} - m_{F814W}$ colors, which suggests that it may be a real feature. The lower panels of the figure adopt the four-group subdivision and the iGC group becomes responsible for the intermediate peak.

7. THE GLOBULAR-CLUSTERS SPATIAL DISTRIBUTION

It has long been known that the red GCs of M 87 are more centrally concentrated than the blue ones (see, e.g., Strader

et al. 2011), but previous studies have mostly focused on the clusters' 1D (radial) surface-density profiles. In this section we investigate the 2D spatial distribution of M 87 GCs, looking for possible (a)symmetries in the density maps.

We analyzed the spatial distribution of GCs in two ways: first we simply divided GCs into the two classical red and blue groups, as in panel (a2) of Figure 6; then, we adopted the 4-group subdvision as defined in panel (b) of Figure 5. In both cases, we focus only on GCs above the 50% completeness limit in the m_{F814W} vs. $m_{F606W} - m_{F814W}$ CMD, which corresponds to $m_{F814W} \lesssim 23.9$ mag. By exploring the spatial distribution of GCs using both the classical and the 4-group division, we might learn something more about the nature of iGCs and fGCs, e.g.: are iGCs and fGCs two new GC groups, or are they just subsamples of the classical blue/red components?

Let us start from the results of the classical subdivision. Since blue/red GCs are defined on the $m_{F606W} - m_{F814W}$ without making use of the UV information, to improve the statistical significance, we included in the analysis all GCs regardless of whether they also have a m_{F275W} measurement. This way, the number of GC above the 50% completeness cut is 1698. Panel (a1) of Figure 7 shows the optical CMD for

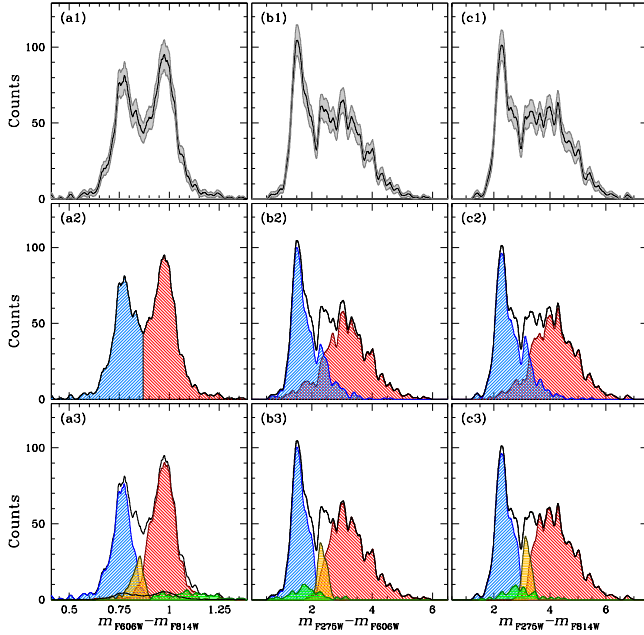$m_{F606W}-m_{F814W}$ $m_{F275W}-m_{F606W}$ $m_{F275W}-m_{F814W}$

Figure 6. Top panels: Histograms of the GC color distributions, with Poisson-based confidence regions (in grey). The same histograms (in black) are divided into the classical blue/red GC component in panel (a2), and color-coded accordingly in (b2) and (c2). In the bottom panels we employed the 4-group subdivision introduced in Fig. 5. See the text for details.

these GCs. The horizontal line marks the 50% completeness cut. Rejected GCs are plotted in grey. Panel (b1) of the figure shows the blue/red GC subdivision, which is made in the same way as in panel (a2) of Figure 6 (the only difference being the 50% completeness cut).

To derive the GC density maps we proceed as follows. For each GC in the two samples we counted the number of surrounding GCs belonging to the same sample within 1800 pixels ($36''$). This radius was chosen by trial and error as a compromise between the need of a fine spatial-distribution mapping and an adequate Poisson statistics. Larger radii would tend to produce very smoothed maps, washing out most of the intrinsic spatial substructures. On the other hand, smaller radii tend to produce noisy maps, dominated by small-number statistics.

Panels (c1) and (d1) of Figure 7 show the resulting 2D density maps, for the blue and the red component, respectively. Each point in these panels represents the location of selected GCs with respect to the center of M 87, and it is color-coded according to the number of surrounding clusters. Colors range from purple (low-density) to green (average) to red (high-density). The center of M 87 is marked by a black cross and was identified as the brightest central pixel in the F275W stack (being the center of M 87 heavily saturated both in F606W and F814W stacks). The direction of the jet is also shown by a black arrow.

While the rGC density map appears to have a Gaussian-like shape, roughly centered on M 87, the density map of bGCs appears to be more asymmetric, and it is flattened in the direction perpendicular to the jet. So, there is a hint for bGCs being preferentially located about a *galactic plane* roughly perpendicular to the jet. The 1D radial profiles of both samples are also shown, in panel (e1), for completeness.

For the second test we use additional information from F275W photometry (in order to divide GCs into four groups), thus lowering the total number of available GCs to 1334

(those above the 50% completeness cut). The optical CMD of selected GCs and their color-distribution are shown in panels (a2) and (b2) of Figure 7. Unfortunately, the small number of iGCs and fGCs (107 and 49 objects, respectively) does not allow us to derive reliable 2D density maps, and we can only compute 1D radial distributions for them.

As was done for the previous test, for each bGC and rGC we counted the number of surrounding GCs belonging to the same population within 1800 pixels. The resulting density maps are shown in panels (c2) and (d2) for bGCs and rGCs, respectively. The available field-of-view (FoV) is now smaller than that of the first test because of the smaller FoV of our WFC3/UVIS images with respect to those of the ACS/WFC. For both blue and red clusters, in the centermost regions the new contours are more flattened than in the case of the previous test (and the effect is more evident for the blue GCs), whereas the GC distribution in the outer regions does not show a significant flattening. This may suggest that iGCs (that were removed in this test) may have a more symmetric distribution than blue and red GCs[7].

It is now more evident that in the centermost regions bGCs (and, to a lesser extend also rGCs) are flattened in a direction nearly parallel to the jet. In order to better quantify this behavior, we least-squares fitted with ellipses the contours of panels (c2) and (d2) to estimate ellipticity and orientation of each contour. The angle $\Delta\theta$ between the jet and the minor axis of the ellipses, and their ellipticities, are reported in Table 1. The outer contours suffer from edge effects caused by the square FoV and by the way we constructed the density maps. As a consequence, ellipticity and orientation for the two outermost contours ($r \gtrsim 80''$) are not reliable and in Table 1 are reported in parenthesis. The distribution of both red and blue GCs is more circular at larger radii, and becomes steadily flatter towards the center. The central flattening of blue GCs is about 50% larger than that of red GCs. The orientation of the fitted ellipses for the red GCs is approximately parallel ($\sim -8°$) to the jet within $r \sim 80''$. On the other hand, the orientation of the ellipses for the blue GCs changes from being parallel to the jet to being almost perpendicular to it when moving outward. The agreement among independent contours, i.e. any contours separated by more than the region over which the cluster-density was assessed, provides a sense of the reality of the differences between blue and red GC subsystems.

Comparing ellipticity and position angle of blue and red clusters with those of M 87 isophotes (from Liu et al. 2005) we find that the ellipticities of the GC distributions follow those of the isophotes in the outer regions of our survey ($\sim 80''$), but then the GC distributions become significantly flattened toward the center whereas the behavior of the isophotes is opposite, becoming even more circular within the central $20''$. The orientation of flattening of red and blue GCs is broadly consistent with that of the outer isophotes of M 87.

The radial profile of all four groups of GCs is shown in panel (e2). The iGC-supbopulation profile (in yellow in panel e2) is remarkably similar to that of the bGCs, suggesting that the iGCs might actually belong to the bGC component, instead of being a separate group.

A special reference needs to be made for the fGC group. They not only have a unique behavior in the CMDs, but they also appear to be the most concentrated group of GCs. It is hard to distinguish whether this indicates their intrinsically

---

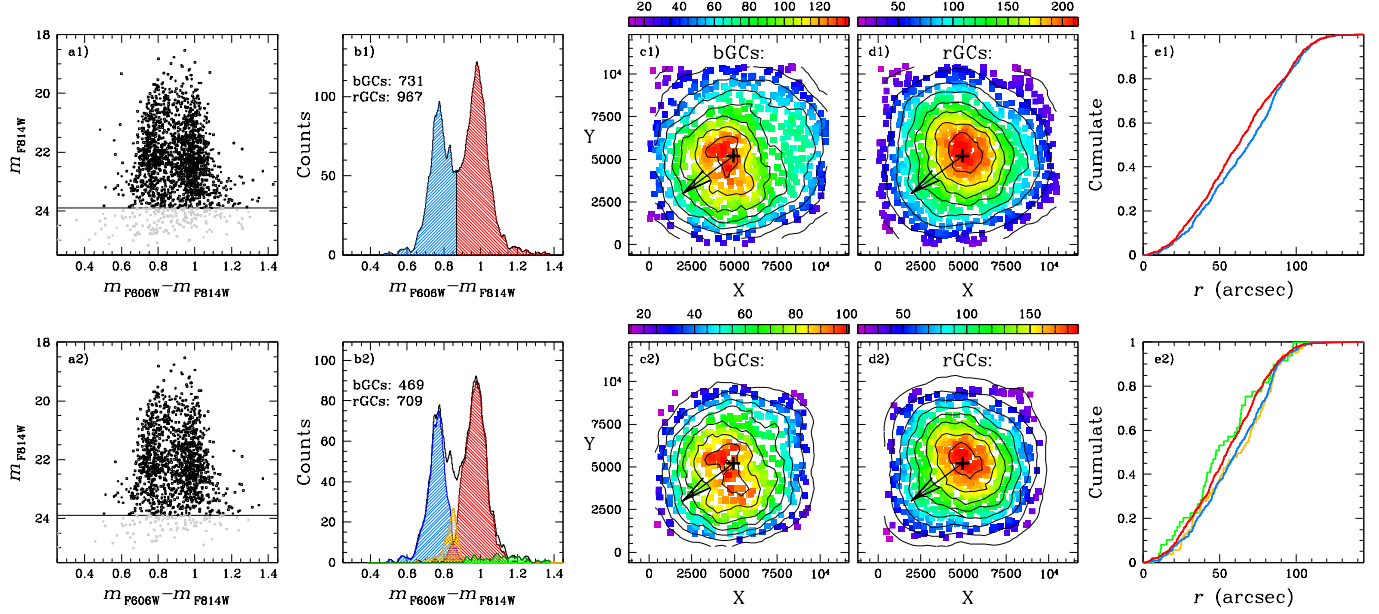[7] The small number of iGCs does not allow us to derive for them a meaningful density map

Figure 7. Two-dimensional distribution and radial profiles of M 87 GCs. Top panels refer to the classical blue/red components, while bottom panels are for the 4-group subdivision. Panels (a) and (b) show the CMD and color histogram of selected stars. Panels (c) and (d) show the spatial distribution of bGCs and rGCs in the two cases, each with linear-scaled contour levels. The radial profile of each GC component is in panels (e).

different nature or whether they have larger photometric errors (especially in the F275W band) as on average they project over a brighter galaxy background.

This flattening near the center of the GC distribution is quite intriguing indeed, and perhaps even more so that the distribution of blue GCs is more flattened than that of the red ones. At first, one would have expected the contrary, with the older, metal-poor component to be dynamically hotter because of the past merging history of M 87. However, we cannot exclude that the difference in flattening, although appreciable, could also arise from a statistical fluctuation given the relatively small number of objects involved in the flattening (only 115 bGCs and 200 rGCs in the central $\sim 40''$) and the necessary smoothing applied to construct the density maps.

Given the flattening in the direction of the jet (hence presumably lying in the equatorial plane of the central supermassive black hole) this flattening may represent a vestige of an earlier disk morphology of M 87. However, the galaxy-core dynamics is typical of massive, non-rotating galaxies which have been built up by merging (see, e.g., Figure A1 in Emsellem et al. 2011). Alternatively, rather than a residual characteristic of the formation of these GCs, the flattening may have been acquired in the course of the dynamical evolution of the GC system. For example, one possibility is that clusters in more radial orbits may have been destroyed by tidal interactions with the supermassive black hole. We are not in the position to discriminate between these options and we leave this as an interesting open issue.

8. COMPARISON WITH MILKY WAY GLOBULAR CLUSTERS

A direct comparison with MW GCs, where the multi-population phenomenon is now well documented, is mandatory if we are searching for signs of multiple stellar populations in the GCs of M 87. There are two *HST* Treasury Programs that made use of the very same detectors and filters used in this work: GO-10775 (PI: A. Sarajedini), which observed 65 MW GCs through ACS/WFC F606W and F814W filters (Sarajedini et al. 2007), and GO-13297 (PI: G. Piotto, Piotto et al. 2015), nearly finished and targeting the cores of

TABLE 1
ELLIPSES PARAMETERS (INNER TO OUTER)

bGCs			rGCs		
Ellipticity	θ (deg)	Major axis ($''$)	Ellipticity	θ (deg)	Major axis ($''$)
0.54	13	32.6	0.34	-7	22.4
0.36	16	50.6	0.20	-6	38.9
0.20	8	60.9	0.20	-6	51.2
0.10	30	70.5	0.12	-10	60.4
0.06	55	79.4	0.09	-8	70.4
(0.07)	(72)	(89.5)	0.04	-17	79.4
(0.07)	(88)	(101.6)	(0.03)	(-34)	(90.5)
			(0.01)	(-38)	(103.8)

46 out of the GO-10775 65 GCs in three WFC3/UVIS filters, including F275W. Additionally, images in F275W for other 12 MW GCs have been acquired with two pilot programs to GO-13297: GO-11233, GO-12311 and GO-12605 (both PI: G. Piotto). Moreover, the core of ω Cen was chosen as WFC3/UVIS calibration field, and have F275W exposures. At the completion of GO-13297 the total number of clusters for which WFC3/UVIS F275W and ACS/WFC F606W and F814W data exist will be 59: about a third of the total number of GCs in the Milky Way.

In order to directly compare MW GCs with those in M 87 we need to: (1) estimate the total light of MW GCs in the three bands; (2) apply reddening corrections in order to have the same reddening of M 87 ($E(B-V) = 0.04$, obtained by multiplying by 1.35 the quoted value $E(V-I) = 0.03$ of Harris 2009); and (3) bring all MW GCs to the same distance of M 87 (distance modulus $(m-M)_0 = 31.0$, again from Harris 2009).

To estimate the integrated total light of the MW GCs we proceeded as follows. First of all, we note that all GO-10775 catalogs are reasonably complete (50%) down to about 5.5 magnitudes below the turnoff, and have comprehensive artificial-star tests that allow proper incompleteness estimates. A direct sum of the flux of the cluster members present in these catalogs, within a certain radius, is therefore a good estimate of the total cluster flux within that radius. While we will inevitably lose a sizable fraction of stars fainter than,

say the 50% completeness limit (especially near the cluster center). the dim light of these missed faint sources will only marginally affect the estimated total light of the clusters and will have an even smaller impact on the inferred integrated colors.

In fact, using artificial-star tests, we estimated the amount of light lost from missed stars in F606W and F814W down to the 50% completeness level and found it to be on the order of 4% in both filters and in nearly all GO-10775 clusters[8]. (This value necessarily varies spatially, and the light lost in the core due to crowding effects is higher than in the outer regions. On average, we found a relative 2% increase in lost flux within the centermost 25″ with respect to the 50″ to 70″ radial interval.) A 4% difference in total flux corresponds to about 0.04 magnitudes. The average $m_{F606W} - m_{F814W}$ color variation due to incompleteness is then found to be of the order of only 0.003 magnitudes. We also computed the total light of 10 randomly-selected clusters as provided by stars down to 2, 4 and 6 magnitudes below the turnoff. On average, the total clusters' light decreased by 0.029, 0.005 and 0.0004 magnitudes for the 2, 4, and 6 mag cuts in F606W, and by 0.034, 0.007 and 0.0007, respectively, in F814W. The difference in the $m_{F606W} - m_{F814W}$ color is then 0.004, 0.002 and 0.0003 for the three magnitude cuts, and therefore negligible. Given this very small impact of incompleteness on the total clusters' light and optical colors, we decided to ignore completeness effects in our calculations.

To obtain stellar fluxes in F275W we used the catalogs of GO-10775 as an input, and fitted F275W library PSFs to each listed stellar position, so that every source in the GO-10775 catalogs will also have a F275W measurement if detected in this band (Soto et al. in preparation). We do not yet have artificial-star tests for the GO-13297 data. Nevertheless, in F275W we can easily detect stars down to 3–4 magnitudes below the turnoff, i.e. 10 magnitudes below the HB (in F275W). This typically translates into about 2.5 magnitudes below the turnoff in F606W, and we already saw that below this cut we lose only a marginal fraction of light in the F606W passband. The missed stars are faint, red MS stars that already have little/no contribution to the clusters light in optical, and even less in F275W. Unfortunately, this is not the case for the two interesting clusters NGC 6388 and NGC 6441, the most metal rich clusters with evidence of helium-rich EHB stars (e.g., Bellini et al. 2013). These heavily reddened Bulge clusters would have required a disproportionate number of *HST* orbits to reach an F275W depth below the turnoff similar to that of the other clusters. Actually, the data barely reach the turnoff, which is a significant contributor to the UV light especially in metal-rich clusters, see Figure 10. Therefore, these clusters are not included in our present analysis.

For the calculation of the total clusters light we selected only bona-fide cluster members, on the basis of their proper motions (obtained as the difference in stellar position between the GO-10775 and GO-13297 catalogs) and on their location on the color-magnitude diagram. These two selection criteria work very well for all clusters except for NGC 6715. In this case, it is impossible to separate cluster members from the core of the Sagittarius dwarf spheroidal galaxy using proper motions, but at least the CMD selections allowed us to remove Sagittarius RGB contaminants.

Needless to say, the FoV of GO-13297 catalogs ($\sim 2.7 \times 2.7$

[8] Specifically, 3.9% (semi-interquartile of 2.0%) for F606W, and 4.2% (semi-interquartile of 1.8%) for F814W.

arcmin^2) is smaller than the tidal radius of MW GCs. To convert our FoV-limited fluxes into the total cluster light, we made use of the fraction-of-light radii listed in Trager, King & Djorgovski (1995). In Their Table 2, the authors report the value of r_{10}, r_{20}, r_{30}, r_{40}, $r_h = r_{50}$, which are the radii within which the 10% to 50% of the total cluster light is enclosed. For each MW GC in our sample, we summed the flux of all the stars within the largest value r_X (where X is one of the listed fraction-of-light radii) that was still fully enclosed in the GO-13297 FoV. These r_X-based fluxes were then accordingly rescaled to synthesize the total clusters light in each of the three passbands. Note that we applied the same scaling factor for UV and optical magnitudes. If UV light and optical light have different radial gradients, this might introduce a bias. Some of our MW clusters are not listed in Trager, King & Djorgovski (1995); we could compute integrated clusters lights for only 45 objects.

We adopted the reddening values listed in Harris (1996, 2010 edition), in order to adjust our integrated magnitudes to the reddening of M 87, by using the extinction coefficients of Sirianni et al. (2005) for ACS/WFC. To date, no official extinction coefficient is available for the F275W filter on the *HST* website. We adopted the value $A_{F275W} = 6.14$, obtained with YES, the York Extinction Solver, using the reddening laws by Cardelli, Clayton & Mathis (1989).

Finally, we corrected the integrated and (de)reddened magnitudes for the difference between the MW GCs distance moduli (from Harris 1996, 2010 edition) and that of M 87 $((m-M)_0 = 31.0$, Harris 2009). The integrated, absolute and de-reddened photometry for MW GCs is listed in Table 2.

Figure 8 shows the three CMDs (panels a, b and c) and the two-color diagram (panel d) of M 87 (in black) and the 45 MW GCs (in red), for which we already have the data in all three passbands. Outstanding MW GCs in the figure are tagged. Note that none of the 45 MW GCs fall on the bulk of the red sequence of M 87 in $m_{F606W} - m_{F814W}$. The metal-rich GC 47 Tuc ([Fe/H]=−0.72, from Harris 1996, 2010 edition) lies just in the middle between blue and red M 87 clusters in the optical color, and just makes it on the red sequence when the color is based on the F275W filter.

Moreover, we note that ω Cen itself would be among the brightest GCs in M 87. Indeed, only a handful of M 87 GCs in our survey field are brighter than ω Cen, but not by much more than 1 magnitude in either m_{F606W} or m_{F814W}. It appears that the most luminous GCs in M 87 are likely siblings of G 1 (Mayall II) in M 31, with a mass of $\sim 10^7$ M$_\odot$ (Ma et al. 2009). The integrated color of NGC 6715 (M 54) is somewhat more uncertain, as this cluster is deeply embedded within the nucleus of the Sagittarius dwarf spheroidal galaxy, in such a way that there are a comparable number of cluster and galaxy stars (that are redder, on average) even in the centermost few arcmin from the cluster center.

From panels (b) and (c) in Figure 8 we note that the bulk of MW and M 87 blue clusters have approximately the same $m_{F275W} - m_{F814W}$ color, but in the two-color diagram shown in panel (d) there is a systematic offset in $m_{F606W} - m_{F814W}$ of ~ 0.06 mag, also appreciable in panel (a). Several sources of error affect our MW GC photometry: errors in the photometric zero-pointing, in the total flux estimate, in the M 87 distance modulus, in the adopted reddening values, and in our estimate of the total clusters' light. We can exclude faint star incompleteness of our MW GC database as the cause of the shift, as this 0.06 mag difference is much bigger than what would possibly be expected from such an effect, as estimated above.
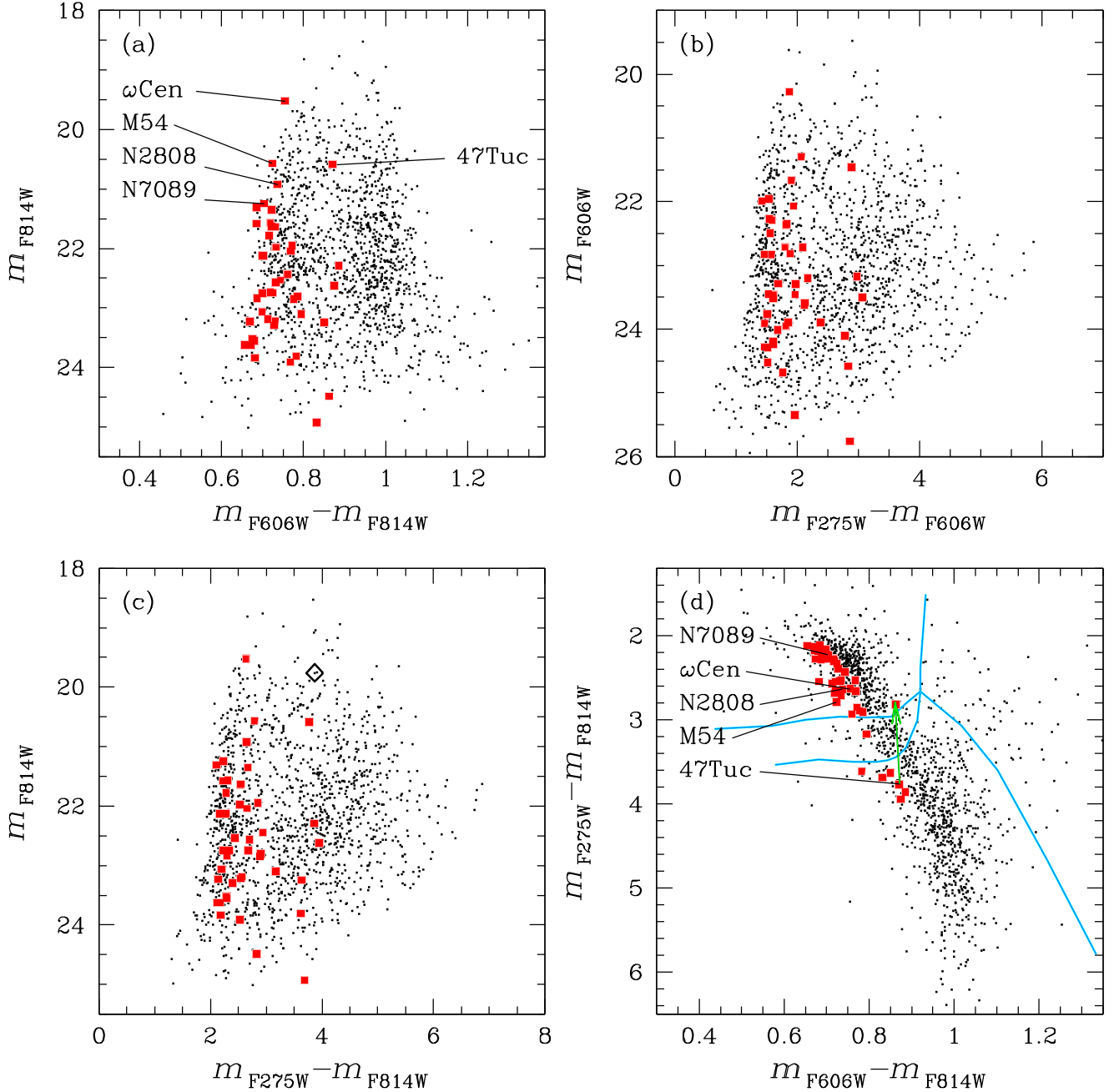
Figure 8. Color-magnitude diagrams and two-color plot for the integrated light of M 87 GCs (black points) and for 45 MW globulars (red squares). Some MW globulars are tagged for clarity. The diamond in panel (c) indicates the cluster with very blue FUV–F275W color, and is discussed in Section 10. The blue lines in panel (d) are the same as panel (b) of Fig. 5. The green arrow is discussed in Sect. 8.2

Another possibility is that the $m_{F606W} - m_{F814W}$ color of MW GCs may have been underestimated given that the brightest RGB stars (above the HB level) tend to be saturated in the GO-10775 images. The photometry of these RGB stars was corrected for saturation effects, but certainly the result cannot be as accurate as in the case of unsaturated stars. Whether this is the reason for the 0.06 mag difference could in principle be ascertained, but it requires a non trivial effort and we wish to postpone it to a future paper. Some of these sources of systematic errors affect our three photometric measurements in the same way, but others may indeed generate a systematic color difference between MW and M 87 clusters. At this stage, we cannot determine whether this difference in color of

~ 0.06 mag is an intrinsic property of MW and M 87 GCs or it is due to systematic errors.

In analogy to the result of S06 and K07, we find that M 87 GCs appear systematically bluer than MW GCs in the color-color plot, at fixed optical color. However, the blue GCs in both galaxies span the same range of colors in $m_{F275W} - m_{F814W}$, hence we attribute the offset to the $m_{F606W} - m_{F814W}$ color, i.e., M 87 GCs do not appear to be *more ultraviolet* than MW GCs. Our data do not allow us to exclude this offset being due to systematic/calibration errors. We note that this color shift was more prominent in S06 and K07 FUV−optical color rather than in the NUV−optical color. The STIS NUV passband used by S06 and K07 partly overlaps
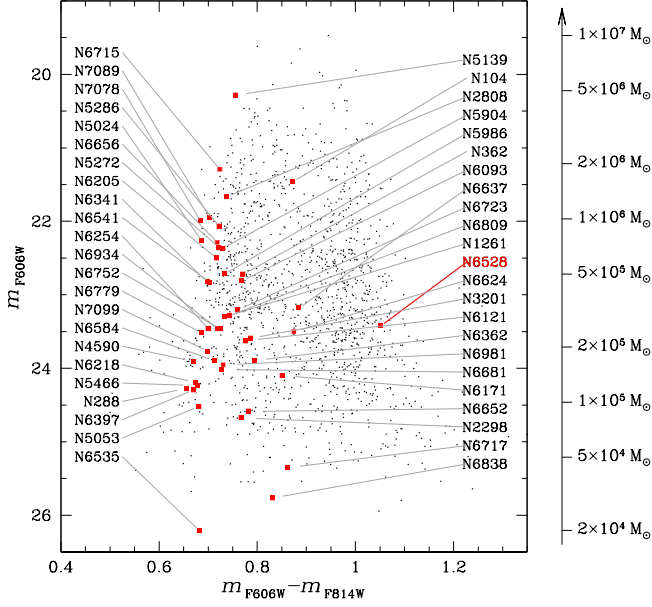
Figure 9. The optical color-magnitude diagram of GCs in M 87 (black points) and in the MW (red squares). In addition, the integrated magnitude and color of the Galactic bulge, metal rich cluster NGC 6528 is reported, using the astro-photometric catalog of Brown et al. (2005).

with the F275W passband, but the FUV passband is even bluer than the bluest WFC3/UVIS filter: F225W. Such a FUV passband would indeed be more sensitive to the bluest HB stars. In Section 10 we shall return on the comparison with S06 and K07 results.

The fact that the vast majority of the MW GCs in our sample occupy the blue half of the M 87 GCs in all the three CMDs should not come as a surprise. The GO-10775 treasury program (and therefore also the GO-13297 one) did not include heavily-reddened clusters, which are generally harbored in the Galactic bulge. These clusters are metal rich and also intrinsically red.

In the Milky Way Bulge there are some extremely-metal-rich clusters that may lie well within the rGC sequence of M 87. To verify this, we additionally estimated the integrated light of NGC 6528 ([Fe/H]=−0.11, $E(B-V)=0.54$, from Harris 1996), an almost solar-metallicity GC in the Bulge, following the very same procedures and selection criteria used for the other clusters. NGC 6528 was observed through ACS/WFC F606W and F814W as part of the GO-9453 program (PI: T. M. Brown, see Brown et al. 2005). This cluster (identified and tagged in red in Figure 9) lies on the red side of the red sequence, as one would expect. So, we cannot claim dramatic systematic differences between color and brightness span of the MW and M 87 GC sequences.

8.1. *Mass estimates for the GCs in M87*

The right side of Figure 9 shows the total-mass scale for the clusters. To estimate the GC masses we assumed the total mass of ω Cen to be 4.05×10^6 M$_\odot$ (D'Souza & Rix 2013), and we linearly scaled this value with the F606W-band luminosities, assuming the same mass-to-light ratio for all clusters. This scale is just a rough estimate of the mass of MW and M 87 clusters, but it should represent a fair first-order mass ranking. For example, the total mass of NGC 6397 is about 1.1×10^5 M$_\odot$ (Heyl et al. 2012), which is about what the scale predicts over an order of magnitude away from the zero point. This implies that at the faint limit (roughly at 10%

TABLE 2
INTEGRATED, REDDENING-FREE ABSOLUTE PHOTOMETRY
OF MILKY-WAY GLOBULAR CLUSTERS

GC ID	m_{F606W}	$(m_{F275W} - m_{F606W})$	$(m_{F275W} - m_{F814W})$
NGC 104	−9.65	2.76	3.60
NGC 288	−6.84	1.33	1.95
NGC 362	−8.40	1.95	2.68
NGC 1261	−7.82	1.84	2.53
NGC 2298	−6.44	1.63	2.36
NGC 2808	−9.45	1.77	2.47
NGC 3201	−7.52	1.98	2.73
NGC 4590	−7.21	1.33	1.96
NGC 5024	−8.85	1.41	2.06
NGC 5053	−6.59	1.38	2.02
NGC 5139	−10.83	1.74	2.46
NGC 5272	−8.76	1.69	2.38
NGC 5286	−9.04	1.81	2.49
NGC 5466	−6.88	1.47	2.11
NGC 5904	−8.75	1.68	2.37
NGC 5986	−8.40	1.67	2.36
NGC 6093	−8.30	1.76	2.49
NGC 6121	−7.49	1.98	2.72
NGC 6171	−7.01	2.65	3.46
NGC 6205	−8.62	1.43	2.10
NGC 6218	−6.92	1.47	2.11
NGC 6254	−7.66	1.39	2.05
NGC 6341	−8.29	1.33	1.99
NGC 6362	−7.22	2.25	3.00
NGC 6397	−6.82	1.38	2.01
NGC 6535	−4.90	1.73	2.38
NGC 6541	−8.29	1.44	2.11
NGC 6584	−7.22	1.72	2.39
NGC 6624	−7.61	2.94	3.77
NGC 6637	−7.93	2.84	3.69
NGC 6652	−6.53	2.70	3.44
NGC 6656	−8.82	1.45	2.13
NGC 6681	−7.09	1.54	2.23
NGC 6715	−9.82	1.93	2.62
NGC 6717	−5.76	1.83	2.65
NGC 6723	−7.91	2.04	2.77
NGC 6752	−7.65	1.48	2.16
NGC 6779	−7.59	1.47	2.12
NGC 6809	−7.83	1.56	2.26
NGC 6838	−5.35	2.73	3.52
NGC 6934	−7.65	1.83	2.51
NGC 6981	−7.16	1.68	2.37
NGC 7078	−9.12	1.29	1.94
NGC 7089	−9.16	1.40	2.06
NGC 7099	−7.34	1.37	2.03

completeness level), we can still detect in M 87 some GCs with masses as low as $\sim 3 \times 10^4$ M$_\odot$ like, e.g., NGC 6717 (Caloi & D'Antona 2011), while even less massive clusters are not included in our sample.

Peng et al. (2009) showed that the brightest M 87 GCs have half-light radii as large as 9 pc, corresponding to $\sim$5.8 pixels on our stacks. A non-negligible fraction of the light of these clusters necessarily falls outside our adopted 7-pixel-radius aperture photometry. Using a 15-pixel-radius aperture photometry, the brightest M 87 GCs are found to be $\sim 35\%$ brighter than with the 7-pixel-based photometry, meaning that they might be up to $\sim 40\%$ more massive than what the mass scale in Figure 9 would predict.
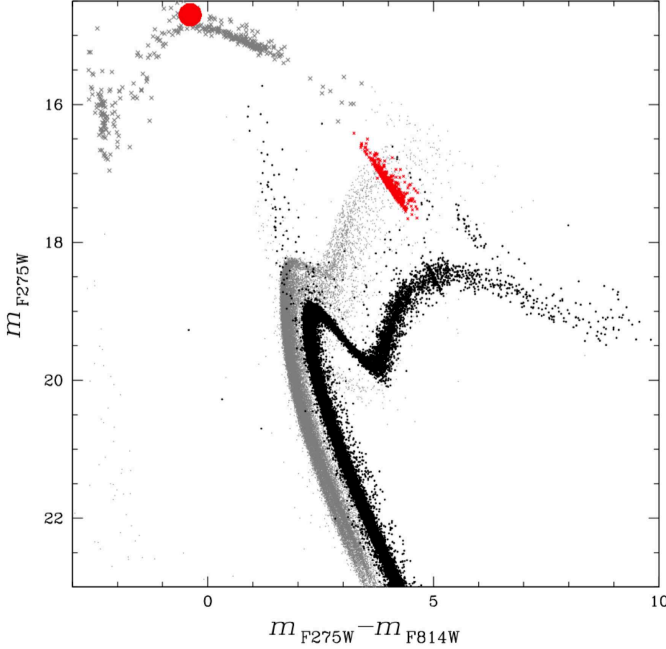
8.2. *UV−optical colors and HB Morphology*

Figure 10. The CMDs of ω Cen and 47 Tuc brought to a common distance (grey and black points, respectively) with the HB stars of 47 Tuc in red. The large red circle shows where all the red-clump stars of 47 Tuc were placed to computed the integrated color differences discussed in the text.

The MW clusters for which we have extensive optical and UV photometry allow us to undertake a simple experiment to quantify the sensitivity of integrated UV–optical colors to the distribution of stars on the HB. Figure 10 shows the m_{F275W} vs. $m_{F275W} - m_{F814W}$ CMD of ω Cen (NGC 5139, grey) and 47 Tuc (NGC 104, black) with the HB stars of 47 Tuc being highlighted in red. Various stellar groups and clumps are recognizable on the HB of ω Cen, corresponding to the many sub-populations of this cluster (see, e.g., Bellini et al. 2010), including the extreme blue *hook* (see also Brown et al. 2010). Notice that the brightest portion of the HB of ω Cen in the F275W band is not the blue hook itself, but instead the next (redder) group of stars, with $m_{F275W} - m_{F814W} \simeq 0$. Thus, a maximum effect on the integrated $m_{F275W} - m_{F814W}$ color would be produced if all HB (red clump) stars of 47 Tuc were moved to this m_{F275W} brightest portion of the HB, as indicated by the red circle in Figure 10. By doing so, i.e., by moving all HB stars from their actual location to the red circle, the synthetic colors of 47 Tuc become ~ 0.01 mag bluer in $m_{F606W} - m_{F814W}$ and ~ 0.98 mag bluer in $m_{F275W} - m_{F814W}$ with respect to the untouched cluster. These new colors would place 47 Tuc near the $m_{F275W} - m_{F814W}$ bluest rim of the M 87 distribution in the two-color plot of Figure 8. The green arrow in Fig. 8d illustrates where 47 Tuc would be placed according to this shift. The new position on the two-color plot is very close to that of NGC 6717, a cluster with a blue HB and no red clump (see, e.g., Fig. 29 of Piotto et al. 2015). We emphasize that these synthetic color shifts necessarily overestimate the possible effect of secondary, helium-enriched populations, as these may represent only a fraction, even if a major one, of the entire stellar content of a GC.

Thus, a substantially smaller $m_{F275W} - m_{F814W}$ color shift, of order of ~ 0.5 mag, is to be expected if –say– only $\sim$half of a cluster population were to populate the brightest portion of the HB in the F275W passband. This is a shift comparable to (or smaller than) the dispersion of the M 87 GC sequences,

see panel (c) of Figure 8.

A larger effect is to be expected when a bluer UV passband is considered. We then repeated the same 47 Tuc experiment using the F225W passband, with the result that the $m_{F225W} - m_{F814W}$ color shift is ~ 1.86 mag, hence this color is substantially more sensitive to the presence of helium-enriched, blue HB stars belonging to a cluster's second stellar generation.

9. COLOR GRADIENTS

One important clue as to how the multiple populations may have originated is given by the spatial distributions of the different populations, which might retain information about their formation sites. Among the massive MW GCs, the second generation is generally more concentrated towards the center of the cluster compared to the first generation (see, e.g., Bellini et al. 2009; Milone et al. 2012a). As such, spatial gradients represent a fossil record of the cluster's dynamical history. This finding has indeed promoted the *cooling flow* model of D'Ercole et al. (2010, 2011). Over time, the various stellar generations interact dynamically and may homogenize their radial distribution in those clusters with short relaxation time.

In the case of the Milky Way, only the most massive clusters (e.g., ω Cen, 47 Tuc, NGC 6441) have a half-mass relaxation time long enough (greater than several Gyrs) to still retain some fossil record of different formation sites of first- and second-generation stars. Obviously, it is impossible to resolve M 87 GCs into stars and study their spatial distribution star by star. However, helium-rich second-population stars are bluer than He-normal stars. Thus, the detection of a color gradient in the light profile of individual M 87 GCs would provide an indication for the presence in them of He-rich sub-populations[9].

For this experiment we selected clusters brighter than $m_{F606W} = 22.7$ (corresponding to $\sim 5 \times 10^5$ M$_\odot$) and reasonably bright in UV ($m_{F275W} < 24.0$), so to have a relatively long relaxation time and enough S/N. A total of 214 M 87 GCs satisfied these selection criteria, specifically: 150 bGCs, 30 iGCs and 34 rGCs. If we were to apply the same selection criteria to MW GCs, we would have included just seven among the Treasury GCs: NGC 2808, NGC 5024, ω Cen, NGC 5272, NGC 5286, NGC 6715 and NGC 7089.

At the distance of M 87, 4.6 pc (the typical half-mass radius for the selected GCs) corresponds to about 3 pixels on our stacks, and a 3-pixel-radius aperture photometry was measured for all the 214 selected sources. Typically, the flux of 29 pixels is summed within a 3-pixel radius (depending on the position of the source centroid within the central pixel). We then compared these 3-pixel-radius-based aperture fluxes with those measured in the annulus between 3 and 4 pixels (~ 6.2 pc) (enclosing 20 pixels), to keep similar Poisson statistics.

The flux ratios $F_{r<3}^{F275W}/F_{r<3}^{F814W}$ within the 3-pixel radius were then computed and compared with those between 3-pixel- and 4-pixel-radius apertures $F_{3<r<4}^{F275W}/F_{3r<4}^{F814W}$. The top-left panel of Figure 11 shows these values as a function of the m_{F275W} magnitude for bGCs, iGCs and rGCs (in blue, yellow and red, respectively). iGCs and rGCs have very similar colors within and outside the 3-pixel-radius apertures. bGCs, on

[9] The color of HB stars is also ruled by a cluster's age, metallicity, mass, etc. The degeneracy with mass is broken by selecting the brightest M 87 clusters, while their metallicity can be inferred by the clusters' $V-I$ color. In this experiment we assume all M 87 clusters to have a similar age.
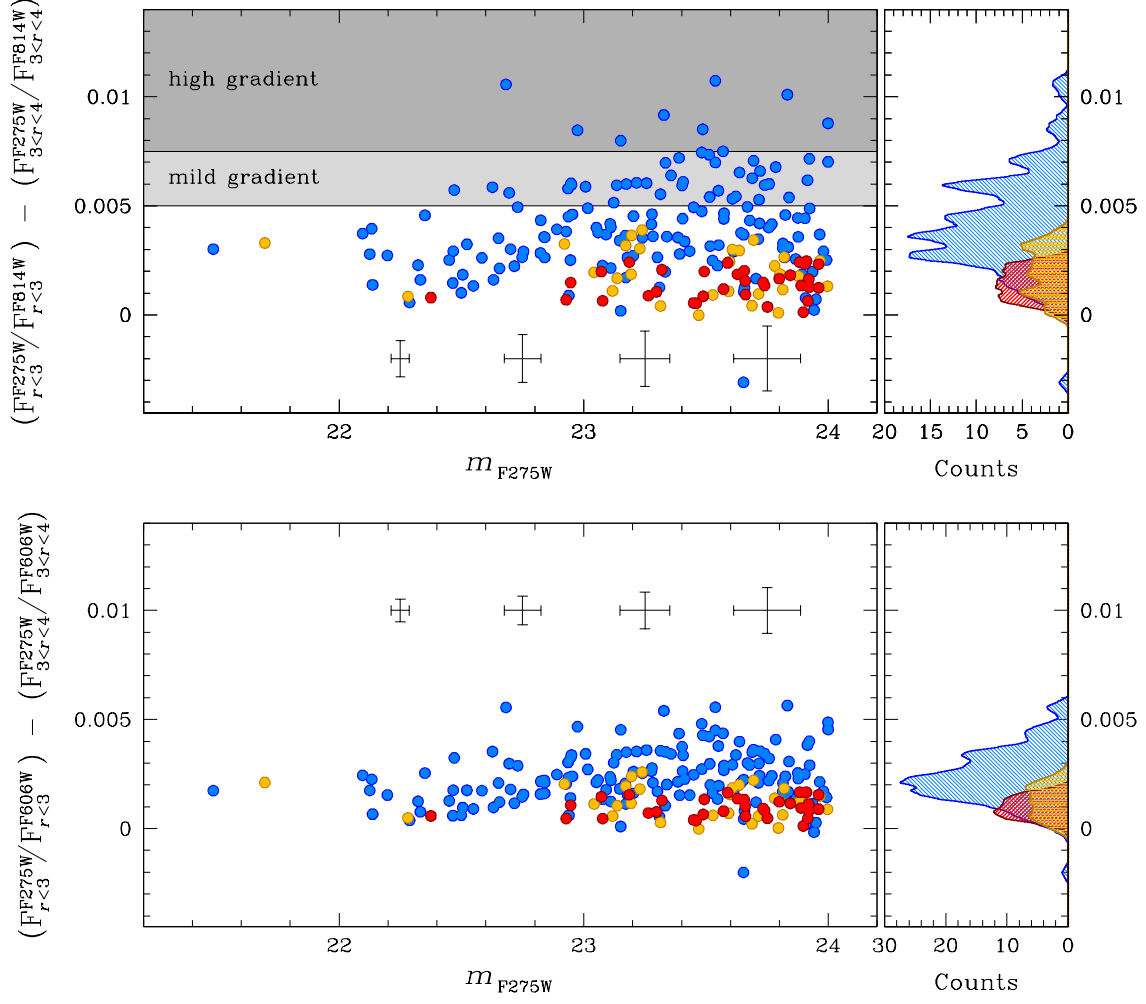
Figure 11. The difference between the UV-to-optical flux ratios within the innermost 3 pixels and that between 3 an 4 pixels from the cluster centers, for the 214 brightest GCs in our M 87 sample. Clusters are color-coded in blue, yellow and red if they belong to the bGC, iGC or rGC sequence, respectively. Error bars show the typical uncertainties for a given m_{F275W} magnitude. The corresponding color-gradient histograms are shown on the right-side of the figure.
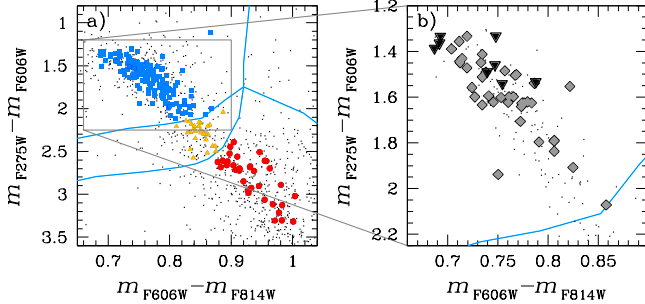

Figure 12. Panel (a): two-color diagram of all M 87 GCs (in black), and of those used for the color-gradient analysis (in blue, yellow and red). A zoomed-in view is in panel (b), where only the analyzed GCs are shown (black dots). Clusters with a mild and a strong color gradient are shown as grey diamonds and black triangles, respectively.

the contrary, have the same color-excess value just as lower limit, and their color is in general appreciably bluer within 3 pixels than outside, with some of them being up to 1% bluer. We highlighted 2 regions in the plot that define bGCs with a mild color gradient (38 GCs, in light grey) and with a higher color gradient (8 GCs, in dark grey). The histogram of the color-excess distribution for bGCs, iGCs and rGCs is shown on the top-right panel (and color-coded accordingly).

As a cross check, we repeated the same exercise using the F606W passband instead of the F814W one. The results are shown in the lower panels of Figure 11. The color differences are now smaller than before, but the trend is still clear. This UV-color excess (or gradient) suggests that a good fraction of bGCs may indeed be hosting He-rich second generation of stars that are still more centrally concentrated than first-generation stars. Other UV-bright sources, like blue-straggler stars, are not a valid explanation: while on one hand they are expected to be more concentrated in the core of GCs, nevertheless they are still 2–3 magnitudes fainter than blue HB stars and substantially less numerous than HB stars among MW GCs (e.g., Ferraro et al. 2003).

Finally, Figure 12 shows the location in the two-color diagram of the clusters used for the color-gradient analysis. Panel (a) shows all M 87 GCs with black points, whereas the 214 selected clusters are color-coded according to their parent population (bGCs in blue, iGCs in yellow, and rGCs in red). The lines used to divide the clusters into subpopulations are also shown in light blue, for clarity. A zoom-in view of the grey box in panel (a) is provided in panel (b), where this time we are plotting only the selected clusters (black dots). Clusters for which we found a mild color gradient are highlighted with grey diamonds, while higher-color-gradient clus-
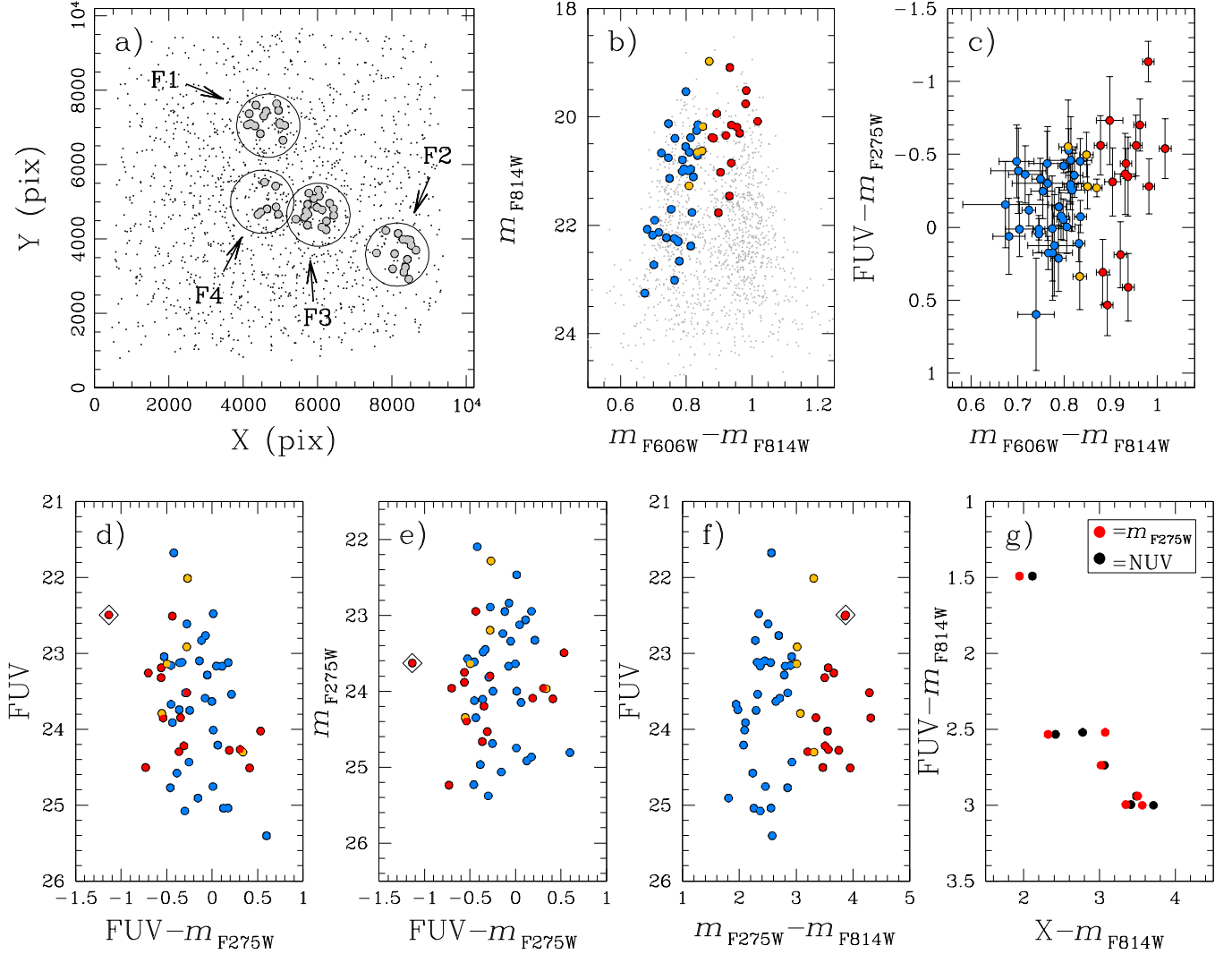
Figure 13. Panel (a): Spatial distribution of S06 GCs cross-identified with our catalog (solid grey). The four fields imaged by S06 are highlighted. (b) The UV-to-optical two-color diagram, with errorbars, for the common sources. The bottom panels show three CMDs employing the FUV photometry. In panels (b) to (f) we color-coded each cross-identified GC according to its parent population. Panel (g) show the correlation between FUV and NUV photometry for common sources in the central field F4, as well as the good agreement between our F275W magnitudes and the NUV measurements of S06. The diamond seen in panels (d), (e) and (f) indicates the cluster with the bluest FUV-m_{F275W} color seen in panel (c).

ters are marked by black triangles. We also checked for the possibility of these color gradients being the result of passband differences in the shape of the PSFs. We found that PSF differences contribute less than $\sim 10\%$ to the "high gradients" seen in Figure 11.

We note that selected bGCs are spread all along the bGC sequence in the two-color diagram of panel (a) of Figure 12, but those displaying a mild color gradient are preferentially found among the bluer bGCs in both $m_{F275W} - m_{F606W}$ and $m_{F606W} - m_{F814W}$ colors. On the other hand, clusters with high color gradients are only found among the bluest M 87 GCs. We conclude that the GCs with both bluest $m_{F275W} - m_{F606W}$ color for their optical color and with a high color gradient represent the best candidates in our sample for hosting helium-enriched sub-populations producing blue HB stars. Note that this is a preliminary exploration of color gradients in these M 87 GCs; a more quantitative analysis would require detailed profile fitting, which is beyond the purpose of the present paper.

10. COMPARISON WITH PREVIOUS FUV–NUV STUDIES

As illustrated in Section 8.2 and Figure 10, the HB of helium-rich GC sub-populations can be very bright in the ultraviolet, potentially making the clusters very blue in integrated UV−optical colors. This is the case for the WFC3 UV filters we have considered, and even more so for the STIS/MAMA FUV passband (1150–1700 Å), that samples substantially shorter wavelengths than either the F225W and F275W passbands. FUV photometry should help us to better characterize the possible presence of such extreme helium-enriched sub-populations, as already been attempted by, e.g., S06 and K07 for M 87 GCs, and by Dalessandro et al. (2012) for MW GCs. Here we want to take advantage of what we have learned so far from our deep F275W, F606W and F814W integrated photometry and extend our analysis to include the FUV. To this end, we cross-identified sources in common between our catalogs and those published in S06 and Dalessandro et al. (2012).

Among the 66 M 87 sources with reliable FUV photometry in S06, only 53 are in common with our catalog. A visual inspection of the missing sources in our stacks revealed that
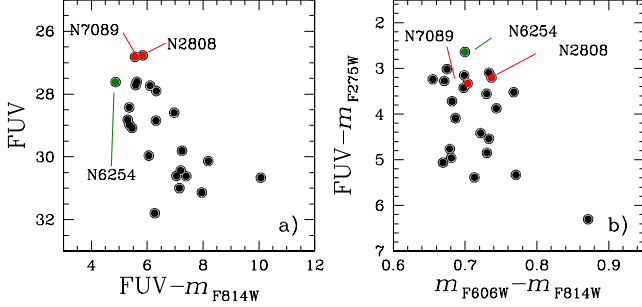
Figure 14. FUV vs. FUV$-m_{F814W}$ CMD (a) and two-color diagram (b) of MW GCs obtained by cross-identifying our MW catalog with the GALEX FUV photometry of Dalessandro et al. (2012). The latter compares to panel (c) of Figure 13, for M 87 GCs.

they are either background galaxies (having a distorted shape in at least one of our stacks), are not found in F814W, or have non-positive flux in F275W. [10]

Panel (a) of Figure 13 shows the FoV of our M 87 field, with all the reliable sources in our catalog as black dots. The four fields imaged by STIS/MAMA are tagged and highlighted with circles. The 53 sources in common with S06 are shown as filled grey circles. Panel (b) shows the optical CMD of all our M 87 GCs (grey dots), and of those cross-identified with S06, color-coded according to their parent population (bGC, iGC or rGC). The two-color diagram employing FUV photometry is presented in panel (c), with photometric error bars. Panels (d), (e) and (f) show three CMDs based on combinations of FUV, WFC3/UVIS and ACS photometry. There is marginal evidence that among these 53 common objects the brightest rGCs are also the bluest in the FUV$-m_{F275W}$ color, with one cluster (highlighted with an open diamond in panels (d), (e) and (f) standing out as the bluest of all. The fact that this cluster is simultaneously red in the optical color and blue in the UV color suggests that it might host two populations: a metal-rich first generation and a He-rich second generation with a very hot HB. As such, it could represent an extreme analog of NGC 6388 and NGC 6441 in the MW. Note that this object is still red when the UV−optical color is based on the F275W filter (panel f), indicating that its HB may be mostly occupied by extremely-hot stars (blue-hook stars in Figure 10). In any case, objects like this one seem to be the exception rather than the rule (1 out of 53). Perhaps more interesting is the fact that most rGCs (and most iGCs as well) are bluer than bGCs in the FUV$-m_{F275W}$ color, whereas they are redder in all other colors. This may signal that indeed these clusters harbor many blue-hook stars.

The central field of S06 (F4 in panel a) also contains photometry in the NUV passband. We have 7 GCs in common between our catalog and that of S06 in this field. Panel (g) of Figure 13 shows the correlation between the FUV$-m_{F814W}$ and X$-m_{F814W}$ colors, where X is either F275W (in red) or NUV (in black). It is worth mentioning the good agreement between our F275W photometry and S06 NUV measurements, despite the different adopted photometric system.

What about our Galaxy? Does the MW have similar GCs compared to the anomalous ones we found in M 87? To find this out, we cross-identified our MW catalog with the inte-

grated GALEX FUV photometry published in Dalessandro et al. (2012). We did not convert their ABMAG values into VEGAMAG, for the same reasons stated above in the case of S06 STMAG.

There are 23 clusters in common between Dalessandro et al. (2012) and our 45 MW GCs discussed in Section 8. In Figure 14 we show the FUV vs. FUV$-m_{F814W}$ CMD on the left (panel a), and the UV-to-optical two-color diagram on the right (panel b). All magnitudes are on the same reference system of M 87 GCs (i.e., the same distance and reddening of M 87, but *not* the same photometric system). The latter diagram should be compared to panel (c) of Figure 13 for M 87 GCs.

The two brightest objects in FUV are, not surprisingly, NGC 2808 and NGC 7089 (M2) in red in both panels[11]. The former cluster has at least three sub-populations with He abundances up to $Y \simeq 0.4$ (Piotto et al. 2007). The latter hosts seven subpopulations with He content up to 0.33, with two sub-populations making $\sim 4\%$ of the cluster being substantially enriched also in iron as well (Milone et al. 2015). Both clusters have a well populated and extended blue HB, with multiple clumps. Yet, they do not stand out for having particularly blue FUV$-m_{F275W}$ or $m_{F275W} - m_{F814W}$ colors. The bluest object in panel (a) of Figure 14 is NGC 6254 (M 10), (marked in green in both panels). This object is also the bluest in FUV$-m_{F275W}$ color. NGC 6254 has a well-populated BHB (see, e.g., Figure 5 of Dalessandro et al. 2013), and the presence of distinct multiple populations within this clusters has just been reported (Piotto et al. 2015).

At odds with M 87 GCs, we find no objects simultaneously red in the optical color and blue in the FUV-based color among these 23 clusters. Moreover, clusters that are red in the optical have about the same UV color (or are even redder) in FUV$-m_{F275W}$ (panel b).

11. DISCUSSION

We have imaged through the UV F275W passband the central $2.'7 \times 2.'7$ field of the giant elliptical galaxy M 87, using the WFC3/UVIS camera onboard the *HST*. In combination with archival ACS/WFC F606W and F814W data covering the same field, we have constructed various optical and UV−optical color-magnitude and two-color plots in an attempt to identify candidate globular clusters hosting a significant helium-enriched sub-population, analogous to those present in several GCs of our own Galaxy, that produce very-blue HB stars. This experiment has attained only partial success. Out of the 1460 candidate GCs identified in all three bands, the best candidates for hosting helium-enriched sub-populations consist of a small group of clusters that are both slightly bluer in $m_{F275W} - m_{F606W}$ for their optical color than MW GCs, and exhibit a UV color gradient.

Using real stellar data for some MW globulars, we have empirically estimated the maximum possible effect on UV−optical colors of a secondary, helium-enriched population. Assuming that such a population makes 50% of the cluster mass, the maximum blueing of the cluster integrated color is ~ 0.5 mag in $m_{F275W} - m_{F814W}$ and ~ 1 mag in $m_{F225W} - m_{F814W}$. This $m_{F275W} - m_{F814W}$ shift is similar to or smaller than the color width of either the blue or the red GC sequence in M 87, hence it does not allow us to unambiguously detect clusters with an exceptionally blue HB. Clearly,

---

[10] We did not convert the FUV STMAG values to the VEGAMAG system because of the lack of a proper photometric conversion between the two photometric systems. This introduces a zero-point offset that is the same for all GCs. Since we are interested here in finding objects that have an anomalous behavior with respect to the average trend, this zero-point offset is of no consequence for our analysis.

[11] The Dalessandro et al. catalog does not provide the FUV photometry for ω Cen.

the $m_{F225W} - m_{F814W}$ color would offer a better chance to do this, but WFC3/UVIS exposures with the bluer F225W filter would have required considerably longer integration times.

For a set of 45 GCs in the MW we have constructed integrated $m_{F275W} - m_{F814W}$, $m_{F275W} - m_{F606W}$ and $m_{F606W} - m_{F814W}$ colors, directly from deep photometry of individual stars that are members of the clusters. After reddening corrections, the UV−optical colors of these MW clusters are compared to those of M 87. We extended the comparison to 53 Milky-Way GCs (but only to F606W and F814W magnitudes), and used them to derive a first-guess estimate of the mass of M 87 GCs.

We included FUV information for 53 M 87 GCs from S06, and found that the brightest rGCs are also as blue as –or even bluer– than the brightest bGCs in FUV−m_{F275W}, with one object being significantly bluer. A similar comparison is made also for 23 MW GCs using Dalessandro et al. (2012) FUV integrated magnitudes. In this case, the bright MW red clusters in optical are not as blue as the bright blue cluster in neither of the colors employing the FUV, at odd with M 87 clusters. Unfortunately, the lack of a statistically-significant sample of metal-rich MW clusters with FUV photometry does not allow us to make a full comparison with the M 87 GC system.

Other results of this investigation include:

- Both red and blue GCs appear to have a slightly flattened distribution, nearly perpendicular to the famous jet, with this flattening being more pronounced for the blue GCs.

- We find that M 87 blue GCs span the same UV−optical color range as blue GCs in the MW. However, they appear to be redder by ~ 0.06 mag in the optical color $m_{F606W} - m_{F814W}$, compared to MW GCs, producing a systematic relative shift in the two-color diagram in qualitative agreement with earlier findings by Sohn et al. (2006) and Kaviraj et al. (2007). However, we cannot exclude that this color shift may result from differences in how colors are measured in the two cluster families.

- Only a handful of M 87 GCs in this survey field appear to be more massive than ω Cen, the most massive cluster in the MW, with some as massive as a few 10^7 M$_\odot$.

- We identify a small sample of M 87 red GCs which are extremely blue in FUV−m_{F275W} (Fig. 13c), which have no known counterparts among the MW GCs (Fig. 14). Such blue colors suggests they may contain a unusual number of extremely blue, helium rich HB stars.

- As a side product, in an Appendix we briefly discuss the images of the jet, counterjet and dust lanes near the center of M 87, which become especially evident in the ultraviolet F275W stack.

We release the photometric catalog of M 87 GCs in the F275W, F606W and F814W bands to the astronomical community, as well as the three high-quality image stacks in the same filters.

REFERENCES

Anderson, J., & King, I. R. 2006, ACS/ISR 2006-01 (Baltimore: STScI) (2006)
Anderson, J., Sarajedini, A., Bedin, L. R., et al. 2008, AJ, 135, 2055
Anderson, J., & Bedin, L. R. 2010, PASP, 122, 1035
Bastian, N.;,Lamers, H. J. G. L. M., de Mink, S. E., Longmore, S. N., Goodwin, S. P. & Gieles, M. 2013, MNRAS, 436, 2398
Bedin, L. R., Piotto, G., Anderson, J., et al. 2004, ApJ, 605, L125
Bellini, A., & Bedin, L. R. 2009, PASP, 121, 1419
Bellini, A., Piotto, G., Bedin, L. R., et al. 2009, A&A, 507, 1393
Bellini, A., Bedin, L. R., Piotto, G., et al. 2010, AJ, 140, 631
Bellini, A., Anderson, J., & Bedin, L. R. 2011, PASP, 123, 622
Bellini, A., Piotto, G., Milone, A. P., et al. 2013, ApJ, 765, 32
Brown, T. M., Ferguson, H. C., Smith, E., et al. 2005, AJ, 130, 1693
Brown, T. M., Sweigart, A. V., Lanz, T., et al. 2010, ApJ, 718, 1332
Busso, G., Cassisi, S., Piotto, G., et al. 2007, A&A, 474, 105
Cardelli, J. A., Clayton, G. C., & Mathis, J. S. 1989, ApJ, 345, 245
Caloi, V., & D'Antona, F. 2011, MNRAS, 417, 228
Ciotti, L., D'Ercole, A., Pellegrini, S. & Renzini, A. 1991, ApJ, 376, 380
Ciotti, L, & Ostriker, J.P. 2001, ApJ, 551, 131
D'Antona, F., & Caloi, V. 2004, ApJ, 611, 871
D'Antona, F., Gratton, R. & Chieffi, A. 1983, Mem.S.A.It. 54, 173
D'Ercole, A., D'Antona, F., Ventura, P., Vesperini, E. & McMillan, S. L. W. 2010, MNRAS, 407, 854
D'Ercole, A., D'Antona, F. & Vesperini, E. 2011, MNRAS, 414, 130
D'Souza, R., & Rix, H.-W. 2013, MNRAS, 429, 1887
Dalessandro, E., Schiavon, R. P., Rood, R. T., et al. 2012, AJ, 144, 126
Dalessandro, E., Ferraro, F. R., Lanzoni, B., et al. 2013, ApJ, 770, 45
de Mink, S. E., Pols, O. R., Langer, N., & Izzard, R. G. 2009, A&A, 507, L1
Emsellem, E., Cappellari, M., Krajnović, D., et al. 2011, MNRAS, 414, 888
Ferraro, F. R., Sills, A., Rood, R. T., Paltrinieri, B., & Buonanno, R. 2003, ApJ, 588, 464
Gebhardt, K., & Kissler-Patig, M. 1999, AJ, 118, 1526
Harris, W.E. 1996, AJ, 112, 1487 (2010 edition)
Harris, W. E. 2009, ApJ, 703, 939
Heyl, J. S., Richer, H., Anderson, J., et al. 2012, ApJ, 761, 51
Kaviraj, S., Sohn, S. T., O'Connell, R. W., et al. 2007, MNRAS, 377, 987
King, I. R., Bedin, L. R., Cassisi, S., et al. 2012, AJ, 144, 5
Krause, M., Charbonnel, C., Decressin, T., Meynet, G., & Prantzos, N. 2013, A&A, 552, AA121
Larsen, S. S., & Brodie, J. P. 2000, AJ, 120, 2938
Liu, Y., Zhou, X., Ma, J., et al. 2005, AJ, 129, 2628
Ma, J., de Grijs, R., Fan, Z., et al. 2009, Research in Astronomy and Astrophysics, 9, 641
Milone, A. P., Bedin, L. R., Piotto, G., et al. 2008, ApJ, 673, 241
Milone, A. P., Piotto, G., King, I. R., et al. 2010, ApJ, 709, 1183
Milone, A. P., Piotto, G., Bedin, L. R., et al. 2012a, ApJ, 744, 58
Milone, A. P., Marino, A. F., Piotto, G., et al. 2012b, ApJ, 745, 27
Milone, A. P., et al., 2015, MNRAS, 447, 927
Norris, J. E. 2004, ApJ, 612, L25
Novak, G. S., Ostriker, J. P. & Ciotti, L. 2012, MNRAS, 427, 2734
Peng, E. W., Côté, P., Jordán, A., et al. 2006, ApJ, 639, 838
Peng, E. W., Jordán, A., Blakeslee, J. P., et al. 2009, ApJ, 703, 42
Piotto, G., Villanova, S., Bedin, L. R., et al. 2005, ApJ, 621, 777
Piotto, G., Bedin, L. R., Anderson, J., et al. 2007, ApJ, 661, L53
Piotto, G. 2009, IAU Symposium, 258, 233
Piotto, G., Milone, A. P., Anderson, J., et al. 2012, ApJ, 760, 39
Piotto, G., Milone, A. P., Bedin, L. R., et al. 2015, AJ, 149, 91
Renzini, A. 1983, Mem.S.A.It., 54, 335
Renzini, A. 2008, MNRAS, 391, 354
Renzini, A. 2013, Mem.S.A.It., 84, 162 391, 354
Rich, R. M., Sosin, C., Djorgovski, S. G., et al. 1997, ApJ, 484, L25
Silverman, B. W. 1986, Monographs on Statistics and Applied Probability (London: Chapman & Hall)
Sirianni, M., Jee, M. J., Benítez, N., et al. 2005, PASP, 117, 1049
Sohn, S. T., O'Connell, R. W., Kundu, A., et al. 2006, AJ, 131, 866
Strader, J., Romanowsky, A. J., Brodie, J. P., et al. 2011, ApJS, 197, 33
Trager, S. C., King, I. R., & Djorgovski, S. 1995, AJ, 109, 218

van Albada, T. S., de Boer, K. S. & Dickens, R. J. 1981, MNRAS, 195, 591   van den Bergh, S. 1967, AJ, 72, 70

APPENDIX

JET, COUNTERJET AND DARK LANES

We briefly comment here on some of the features related to the prominent jet , so evident in the stack images. We may return to some of these issues in the future, but for this paper we are primarily focused on the GC population.

Besides the famous jet of M 87, one obvious counterjet feature is clearly visible in Figure 1, with three other faint filamentary structures being possibly related to the counterjet (such as counterjet-generated shock fronts). The red-green-blue color-scale of this panel is also enhancing the visibility of these dim features. Some of them are bright in F606W (marked as "Green features" in the figure), while others are almost invisible in this band, yet are still bright in the other two bands ("Purple features"). These color differences may be due to different emission-line ratios resulting from different excitations among the features.

The dark areas near the center of M 87 visible in Figure 1 are not an artifact of the galaxy-subtraction routines but are real features in the scene. Figure 15 shows these features in more detail, having been optimized for this purpose. Various dust filaments around the galactic center and the jet are now clearly visible: they are also present in the non sky-subtracted stacks,
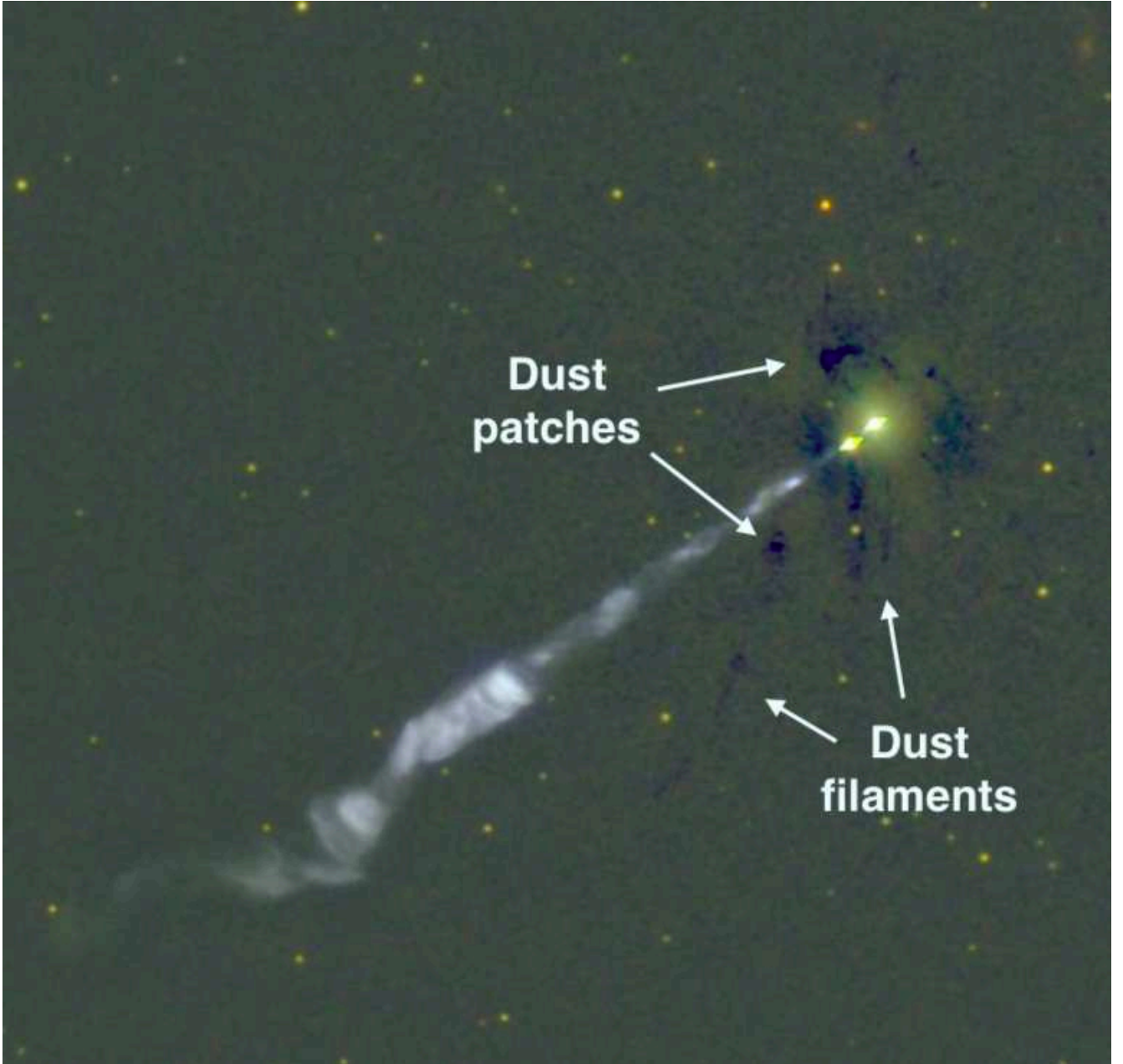

Figure 15. A zoomed-in view of the region around the center of the galaxy and the jet. The color scale has been stretched to enhance filaments and patches of dust.

although they stand out less clearly, due to the scattered light of the galactic core. They are visible in all three bands, but are definitely more prominent in the F275W image, as expected from obscuring dust clouds. Notice also the sharp edges of some of them, with one being clearly in front of the jet and attenuating the light of its obscured section, suggesting they could be the swan song of recent tidally-disrupted dwarf galaxies.

The phenomenology of the M 87 core is typical of what one expects to happen in a very massive elliptical galaxy. Supernova heating at the known rate of Type Ia supernovæ is indeed insufficient to prevent gas outflows to eventually turn to inflows following a central-cooling catastrophe: as stellar mass loss accumulates, the hot gas density increases until cooling exceeds the supernova heating (Ciotti et al. 1991). Under such circumstances, the inflowing material can feed the central supermassive black hole, starting a series of intermittent nuclear activity with duty cycles of several 10^8 yrs (Ciotti & Ostriker 2001; Novak, Ostriker & Ciotti 2012). This kind of recurrent activity is indeed instrumental in keeping the galaxy quenched, once star formation has been quenched for the first time (by whatever mechanism).

Coming back to the dark spots, one interesting question concerns the origin of the obscuring dust. Forming and growing dust in the interstellar medium itself, at the time of the cooling catastrophe near the center, is one option. However, the density may not be high enough for rapid nucleation except perhaps near the black hole itself. Alternatively, dust may form in the wind of mass-losing red giants and AGB stars and survive sputtering just in the cooler gas resulting from the cooling catastrophe. We have no decisive argument either way, other than that these dust features are most probably vestiges of the events that lead to the re-fueling of the central black hole.

One can also notice that bright regions appear in between dark patches. Their intrinsic nature may actually be similar to the dark patches, possibly being dust-rich clouds that shine of dust-scattered light from the AGN itself.